

# Radial measurements of IMF-sensitive absorption features in two massive ETGs

Sam P. Vaughan<sup>1\*</sup>, Ryan C. W. Houghton<sup>1</sup>, Roger L. Davies<sup>1</sup>  
and Simon Zieleniewski<sup>1</sup>

<sup>1</sup>*Astrophysics, Denys Wilkinson Building, Keble Road, Oxford, OX1 4RH*

Accepted XXX. Received YYY; in original form ZZZ

## ABSTRACT

We investigate radial gradients in the stellar initial mass function (IMF) in two early type galaxies using resolved measurements of several far red gravity sensitive absorption features, including the “Wing-Ford” band (FeH). We use the Oxford Short Wavelength Integral Field Spectrograph (SWIFT) to obtain resolved spectroscopic observations of NGC 1277 and IC 843, two nearby galaxies with large central velocity dispersions. Our observations cover the IMF sensitive features sodium NaI0.82, the calcium triplet CaT0.86 and FeH, along with MgI0.88 and TiO0.89. Within both galaxies we measure flat FeH profiles at  $\sim 0.4 \text{ \AA}$  with strong gradients in NaI. If we assume that the IMF takes the form of a single power law (like a Salpeter IMF), we can rule out a large IMF gradient in these objects and attribute the change in NaI absorption to an abundance gradient in [Na/Fe]. We are unable to rule out an IMF gradient in a “bimodal” or multi-segment IMF in either galaxy, since our data do not allow us to investigate the functional form of the IMF below  $1 M_{\odot}$ .

**Key words:** galaxies: stellar content – galaxies: elliptical and lenticular, cD

## 1 INTRODUCTION

The stellar Initial Mass Function (IMF) is of fundamental importance for understanding the evolution and present day stellar content of galaxies. The IMF defines the number density of stars at each mass on the zero age main sequence in a population, and is thus intricately linked to the small-scale, turbulent and not-well-understood process of star formation whilst also defining global properties for the population as a whole. The low mass end of the IMF, and hence the number of low mass stars, greatly affects the mass-to-light ratio ( $M/L$ ) of a system, since a large proportion of the stellar mass in a galaxy comes from stars below  $1 M_{\odot}$ . The fact that these low mass stars contribute so little to the integrated light of a population means that large changes in the  $M/L$  will not necessarily be reflected in large changes to the properties of the light itself. The high mass slope of the IMF makes a contribution to a galaxy’s  $M/L$  ratio too, via stellar remnants, and also defines the importance of stellar feedback and the amount of chemical enrichment that takes place. Furthermore, a form for the IMF is assumed whenever a stellar mass or star formation rate is calculated, and the

implications for such observational parameters if the IMF is not universal could be very serious (e.g Clauwens et al. 2016).

Early efforts to measure the IMF were pioneered by Salpeter (1955), who used direct star counts to parametrize the IMF as a power law of the form  $\xi(m) = km^{-x}$  with an exponent of  $x = 2.35$ . Using a single power law to describe the IMF has come to be called a “unimodal” description. The value of the Salpeter exponent at the high mass end has remained remarkably constant in the numerous studies of our own galaxy since, with modern day IMF parameterisations of the Milky Way incorporating a flattening at low masses: e.g Kroupa (2001) and Chabrier (2003). An IMF with a power law at masses greater than  $0.6 M_{\odot}$ , a flat low-mass end and a spline interpolation linking the two regimes is described as a “bimodal” IMF (Vazdekis et al. 1996). The high end slope of a bimodal IMF is defined by a power law index  $\Gamma_b$ , which is related to  $x$  via  $x = \Gamma_b + 1$ .

Historically, little evidence was found for an IMF in our galaxy which varied depending on parameters such as metallicity or environment (see Bastian et al. (2010) for a review). More recently, however, evidence has emerged for a non-universal IMF in studies of the unresolved stellar populations of ETGs. Dynamical modelling of galaxy kinematics

\* E-mail: sam.vaughan@physics.ox.ac.uk (SPV)

undertaken by the ATLAS3D team (Cappellari et al. 2011) and Thomas et al. (2011b) have shown that the M/L ratios of ETGs compared to the M/L ratio for a population with a Salpeter IMF diverge systematically with velocity dispersion, implying that more massive ETGs have more “bottom heavy” (dwarf enhanced) IMFs (e.g. Cappellari et al. 2013). Comparisons between stellar population synthesis models and strong gravitational lensing predict a similar IMF- $\sigma$  relation (e.g. Treu et al. 2010), although massive ETGs with Milky Way-like IMFs have also been found (e.g. Smith et al. 2015).

This work concerns a third method of studying the IMF in extragalactic objects. Certain absorption features in the spectra of integrated stellar populations vary in strength between (otherwise identical) low mass dwarf stars and low mass giants. A measurement of the strength of these “gravity sensitive” indices gives a direct handle on the dwarf-to-giant ratio and hence the low-mass IMF slope in the population. Important far red gravity sensitive absorption features include the sodium NaI doublet at 8190 Å (Spinrad & Taylor 1971; Faber & French 1980; Schiavon et al. 1997a), the calcium triplet (CaT: Cenarro et al. 2001) and Iron Hydride or “Wing-Ford band” at 9916 Å (FeH: Wing & Ford 1969; Schiavon et al. 1997b). Studying gravity sensitive absorption features in the spectra of ETGs in this way has a long history (e.g. Spinrad & Taylor 1971; Cohen 1978; Faber & French 1980; Couture & Hardy 1993; Cenarro et al. 2003), before more recent work by van Dokkum & Conroy (2010) reignited interest in the topic.

Studies of optical and far red spectral lines have suggested correlations between the IMF and [Mg/Fe] (van Dokkum & Conroy 2012), metallicity (Martín-Navarro et al. 2015c), total dynamical density (Spiniello et al. 2015a) and central velocity dispersion (La Barbera et al. 2013a), but importantly the agreement between spectral and dynamical IMF determination is unclear. Smith (2014) compared the IMF slopes derived using spectroscopic methods in CvD12 and dynamical methods in Cappellari et al. (2013) for galaxies in common between the two studies. He found overall agreement between the two methods regarding the overarching trends presented in each study, but no correlation at all between the IMF slopes determined by each group on a galaxy by galaxy basis. Additional investigation of individual galaxies using independent IMF measurements, rather than comparison of global trends between populations, is required to understand and explain this disagreement.

A more technically challenging goal in spectral IMF measurements is determining whether IMF gradients exist within a single object. Formation pathways of ETGs predict “inside-out growth”, where the centre of a massive galaxy forms in a single starburst event before minor mergers with satellites accrete matter at larger radii (e.g. Naab et al. 2009; Hopkins et al. 2009, and references therein). IMF gradients can naturally arise from such a formation history if the global IMF differs between merger pairs, but few studies have presented evidence for such gradients to date. La Barbera et al. (2016) measure an IMF gradient in a massive ETG with central  $\sigma \sim 300 \text{ km s}^{-1}$ , whilst Martín-Navarro et al. (2015b) report IMF gradients in three ETGs, including NGC 1277 studied in this work (Martín-Navarro et al. 2015a,b, hereafter MN15). Other studies make radial measurements of gravity sensitive indices but conclude in

favour of individual elemental abundance gradients rather than a change in the IMF: see Zieleniewski et al. (2015), Zieleniewski et al. (2017) and McConnell et al. (2016).

In this work, we present radial observations of gravity sensitive absorption features in two galaxies. The first, NGC 1277, is a massive, compact ETG located in the Perseus cluster ( $z = 0.01704$ ). NGC 1277 is a well studied object. It has been named as a candidate “relic galaxy” due to its similarity with ETGs at much higher redshifts (Trujillo et al. 2014), seen controversy over the mass of its central black hole (e.g. see van den Bosch et al. 2012 compared to Emsellem 2013) and had radial measurements of its IMF gradient taken, found using optical and far red absorption indices (MN15). Their study didn’t extend to measurements of the FeH index, however. MN15 found a bottom heavy bimodal IMF at all radii, measuring the slope of the IMF to be  $\Gamma_b \sim 3$  (the same high-mass slope as a unimodal power law with  $x = 4$ ) in the central regions and dropping to  $\Gamma_b \sim 2.5$  ( $x = 3.5$ ) at radii greater than  $0.6 R_e$ .

The second galaxy, IC 843, is an edge on ETG located on the edge of the Coma cluster ( $z = 0.02457$ ). Thomas et al. (2007) conducted a study of the dark matter content of 17 ETGs in Coma, finding that IC 843 had an unusually high mass-to-light ratio in the  $R_c$  band with the best fitting model implying that mass follows light in this system. This result could be explained by a bottom heavy IMF, but also by a dark matter distribution where the dark matter closely follows the visible matter. Both galaxies were chosen because the evidence for their heavy IMFs implies that the Wing-Ford band could be particularly strong in these objects.

This paper is organised as follows. Section 2 summarises our observations describes the data reduction process, including details of sky subtraction and telluric correction. We summarise our radial index measurements in section 5, present our interpretations in section 7 and draw our conclusions in section 8. Appendices contain further discussion of our telluric correction and sky subtraction techniques. We adopt a  $\Lambda$ CDM cosmology, with  $H_0 = 68 \text{ km s}^{-1}$ ,  $\Omega_m = 0.3$  and  $\Omega_\Lambda = 0.7$ .

## 2 OBSERVATIONS AND DATA REDUCTION

We used the Short Wavelength Integral Field specTrograph (Thatte et al. 2006, SWIFT) on January 27th 2016 and March 17th 2016 to obtain deep integral field observations of NGC 1277 and IC 843. Observations were taken in the 235 mas spaxel<sup>-1</sup> settings, giving a field-of-view of 10.3'' by 20.9''. The wavelength coverages extends from 6300 Å to 10412 Å, with an average spectral resolution of  $R \sim 4000$  and a sampling of 1 Å pix<sup>-1</sup>. Dedicated sky frames, offset by  $\sim 100''$  in declination, were observed in an OSO pattern to be used as first order sky subtraction. The seeing ranged between  $\sim 1''$  and  $1.5''$  throughout. Table 1 lists details of the targets and observations.

The wavelength range of SWIFT allows for measurements of the NaI<sub>SDSS</sub>, CaII triplet, MgI and FeH (Wing Ford band) absorption features, as well as MgI 0.88 and TiO 0.89. Definitions of pseudo-continuum and absorption bands for each index, taken from Cenarro et al. (2001) and van Dokkum & Conroy (2012), are given in Table 2. We use the definition of NaI<sub>SDSS</sub> from La Barbera et al. (2013a).

**Table 1.** Targets and Observations

Galaxy	D (Mpc)	Ra	Dec	z	$R_e$ (kpc)	Obs. Date	Integration Time (s)
NGC 1277	74.4	03:19:51.5	+41:34:24.3	0.01704	1.2	27th Jan 2016	$7 \times 900$
IC 843	107.9	13:01:33.6	+29:07:49.7	0.02457	4.7	17th Mar 2016	$9 \times 900$

**Table 2.** Definitions of the feature bandpass and blue and red pseudo-continuum bandpasses for each index studied in this work, from Cenarro et al. (2001) and CvD12. The  $\text{NaI}_{\text{SDSS}}$  definition is from La Barbera et al. (2013a). Since it is a ratio between the blue and red pseudo-continua, the TiO index has no feature bandpass definition. All wavelengths are measured in air.

Index	Blue Continuum ( $\text{\AA}$ )	Feature ( $\text{\AA}$ )	Red Continuum ( $\text{\AA}$ )
$\text{NaI}_{\text{SDSS}}$	8145.2-8155.2	8182.3-8202.3	8235.3-8246.3
CaT	8474.0-8484.0	8484.0-8513.0	8563.0-8577.0
	8474.0-8484.0	8522.0-8562.0	8563.0-8577.0
	8619.0-8642.0	8642.0-8682.0	8700.0-8725.0
MgI	8777.4-8789.4	8801.9-8816.9	8847.4-8857.4
TiO	8835.0-8855.0	—	8870.0-8890.0
FeH	9855.0-9880.0	9905.0-9935.0	9940.0-9970.0

The data were reduced using the SWIFT data reduction pipeline to perform standard bias subtraction, flat-field and illumination correction, wavelength calibration and error propagation. Cosmic ray hits were detected and removed using the LaCosmic routine (van Dokkum 2001).

Differential atmospheric refraction causes the centre of the galaxy to change position within a datacube as a function of wavelength. Although the magnitude of this effect is small (leading to a  $\sim 1''$  shift at red wavelengths for the observations which are lowest in the sky), individual cubes were corrected by interpolating each wavelength slice to a common position. The individual observation cubes were combined using a dedicated python script, which linearly interpolates sub-pixel offsets between the frames.

### 3 TELLURIC CORRECTION AND SKY SUBTRACTION

At the redshift of these galaxies, telluric absorption is prevalent around the MgI and TiO features in both objects and near the blue continuum band of the  $\text{NaI}_{\text{SDSS}}$  feature in NGC 1277. We used the ESO tool MOLECFIT (Kausch et al. 2014) to remove it from our spectra. MOLECFIT creates a synthetic telluric absorption spectrum based on a science observation contaminated by telluric absorption. Using the radiative transfer code of Clough et al. (2005), a model line-spread function of the instrument used to observe the data and a model atmospheric profile based on the temperature and atmospheric chemical composition at the time and place of observation, a telluric spectrum is fit to the science spectra and then divided out. We use MOLECFIT between the regions  $\lambda\lambda$  7561-7768  $\text{\AA}$ , 81212-8338 $\text{\AA}$  and 8931-9875  $\text{\AA}$ .

Variations in night sky emission lines occur on similar timescales to our observations, meaning that significant

residuals from telluric emission remain after first order sky subtraction. This is especially true in the far red end of the spectrum. These residuals are the main source of systematic uncertainty in the measurement of the FeH band, and so must be accurately subtracted to ensure robust index measurements at  $1\mu\text{m}$ . We use two independent sky subtraction methods in this work: removing skylines whilst simultaneously fitting kinematics, and fitting each wavelength slice of our observation cubes with a model galaxy profile and sky image before subtracting the best fit sky model.

#### 3.1 Removing Skylines with pPXF

The first sky subtraction technique uses the method of penalised pixel fitting (Cappellari & Emsellem 2004, pPXF) to fit sky spectra to our data at the same time as fitting the stellar kinematics, as discussed in Weijmans et al. (2009) and Zieleniewski et al. (2017). This involves passing pPXF a selection of sky templates (as well as stellar templates) which are scaled to find the best fit linear combination to the remaining sky residuals.

The sky templates were extracted from the dedicated sky frames observed throughout the night. To account for flexure, each sky template was shifted forward and backwards in wavelength by up to 2.5 pixels (2.5  $\text{\AA}$ ). Note that the pPXF sky subtraction occurs *after* first order sky subtraction, and so we also include negatively-scaled sky spectra in the list of templates in order to fit negative residuals (which correspond to over-subtracted skylines). The sky spectra were also split into separate regions around emission lines caused by different molecular transitions, based on definitions from Davies (2007). We also introduced a small number of further splits to the sky spectrum by eye, around areas where skyline residuals changed sign. Each region was allowed to vary individually in pPXF to achieve the best sky subtraction.

The choice of sky splits makes a noticeable difference to the quality of sky subtraction, especially around the feature most contaminated by sky emission, the Wing-Ford band. Correspondingly, the sky split selection has a non-negligible effect on the FeH index measurement. We selected the total number and location of cuts to the sky spectrum around FeH by quantifying the residuals of the sky subtracted spectrum around the best-fitting pPXF template, for various sky split combinations. We chose the combination of sky splits which had a distribution containing fewest catastrophic outliers (i.e most similar to a normal distribution), both by eye and quantified using the Anderson-Darling test statistic (Anderson & Darling 1954). This process is discussed in further detail in Appendix A.

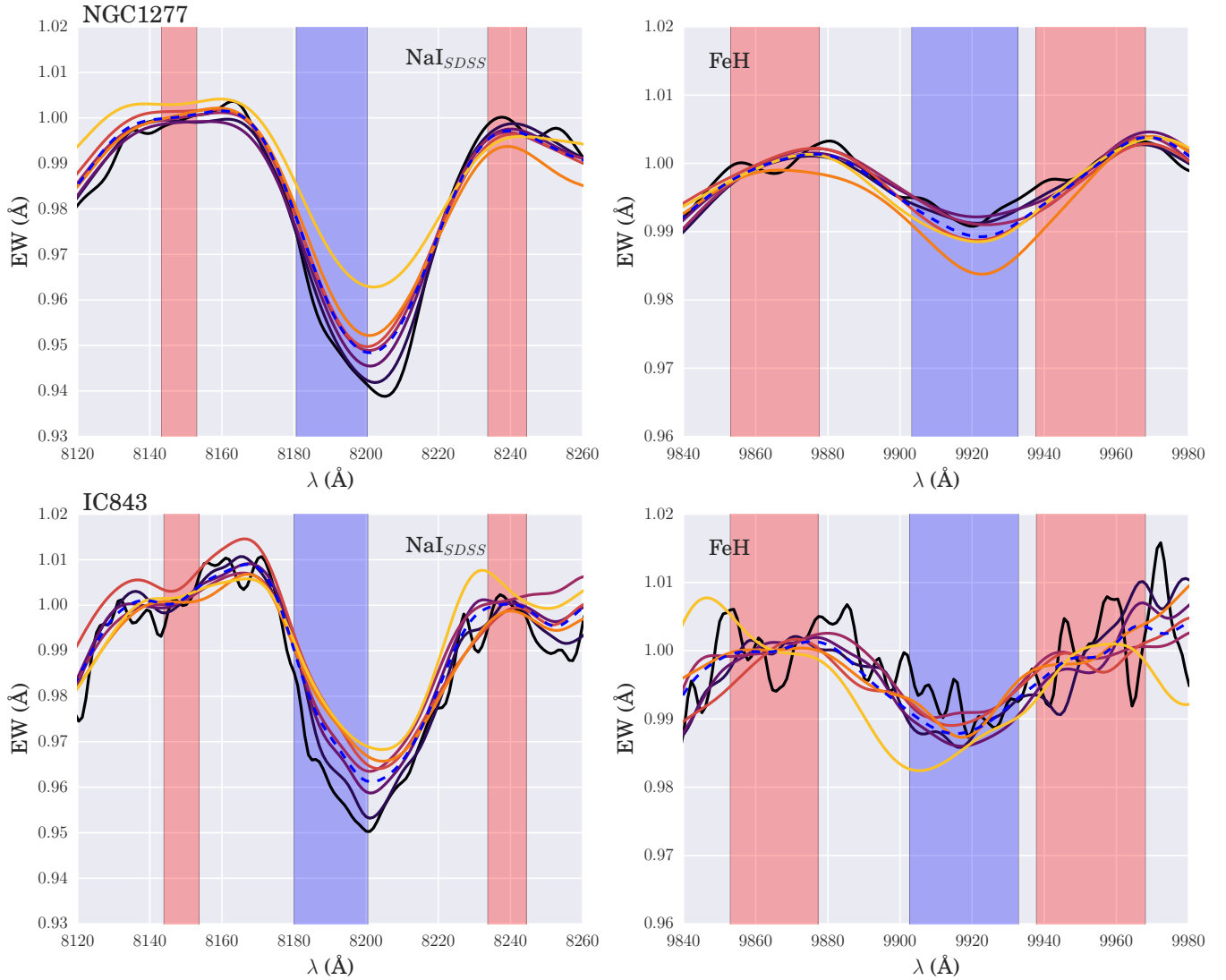


**Figure 1.** Plots of the spectra around the IMF sensitive indices NaI0.82 and Wing-Ford band (FeH) for NGC 1277 (top) and IC 843 (bottom). Spectra are coloured from dark (central bin) to light (outskirts) and are convolved up to a common velocity dispersion of  $450 \text{ km s}^{-1}$  (NGC 1277) and  $300 \text{ km s}^{-1}$  (IC 843) for display purposes only. The dotted blue line is the global spectrum for each galaxy. Blue and red shaded regions show the index band and continuum definitions respectively.

### 3.2 Median Profile Fitting

The second sky subtraction method is independent of the first. Each observation cube (which has undergone first order sky subtraction) is a combination of galaxy light and residual sky light. In each wavelength slice, sky emission corresponds to an addition of flux in all pixels whereas galaxy light is concentrated around the centre of the observation. We aim to model these two contributions in a single data cube and subtract off the best fitting sky model.

We take the median image of the data cube as the galaxy model in our fitting procedure. This assumes that the shape of galaxy light profile doesn't change over the SWIFT wavelength range of  $6300 \text{ Å}$  to  $10412 \text{ Å}$ , but is only scaled up and down as the galaxy gets brighter or dimmer and the instrument throughput varies. The sky model is a flat image at every wavelength slice; the same constant value across the IFU in each spatial dimension.

Using a simple least squares algorithm, we simultane-

ously fit the galaxy and sky model to each wavelength slice of an individual cube. We then subtract the best fit sky residuals for each cube, combine the cubes and are left with an alternative sky subtracted data cube for each galaxy. These are binned and passed to pPXF to measure the kinematics as before, except without using the sky subtraction technique of Section 3.1.

The median profile fitting method leads to slightly noisier results than using pPXF, and as such all index measurements quoted in this paper are derived from the first sky subtraction method. However our conclusions are unchanged regardless of which sky subtraction technique we employ. A comparison of the two methods is presented in Appendix A.

## 4 INDEX MEASUREMENTS

To attain a signal to noise (SN) ratio high enough to robustly measure equivalent widths, we binned the data cubes into

elliptical annuli of uniform SN, which were then split in half along the axis of the galaxy’s rotation. The kinematics in each bin were measured using pPXF, after which each half of the same annulus was interpolated back to its rest frame and added together. This leads to a roughly constant SN in each bin for each index. Spectra of the 3 IMF sensitive indices studied in this work, for each radial bin in both galaxies, are shown in Figure 1.

We also make velocity and velocity dispersion measurements as a function of radius by binning the datacube to a SN ratio of 15 (for NGC 1277) or 20 (for IC 843), then place a pseudo-slit across the cube along the major axis of each galaxy. These are shown in Figure 2, along with the long-slit results from MN15. Both galaxies are fast rotators, with peak rotation velocities reaching  $\pm 300 \text{ km s}^{-1}$  in NGC 1277 and  $\pm 200 \text{ km s}^{-1}$  in IC 843. The central velocity dispersion in NGC 1277 is remarkably high at  $\sim 420 \text{ km s}^{-1}$ , in agreement with the values measured by MN15.

The equivalent widths of absorption features depend on the velocity dispersion of the spectrum they are measured from. A larger velocity dispersion tends to “wash out” a strong feature, leading to a smaller equivalent width. In order to compare measurements between different radii in the same galaxy, as well as between separate galaxies, we correct each index measurement to a common  $\sigma$  of  $200 \text{ km s}^{-1}$  using the same method as Zieleniewski et al. (2017).

Equivalent widths are measured using the formalism of Cenarro et al. (2001), which measures indices relative to a first order error-weighted least squares fit to the pseudo-continuum in each continuum band. We propagate errors from the variance frames of each observation by making a variance spectrum for each science spectrum. All error bars in this work show  $1\sigma$  uncertainties.

#### 4.1 Selected spectral features

The SWIFT wavelength range extends from  $6300\text{\AA}$  to  $10412\text{\AA}$ , covering the IMF sensitive indices NaI0.82, CaT0.86 and FeH0.99. We also make radial measurements of the TiO0.89 bandhead and the MgI0.88 absorption feature.

The sodium feature at  $0.82 \mu\text{m}$  is well studied, with a long history of measurements in the context of IMF measurements (e.g. Spinrad & Taylor 1971; Faber & French 1980; Schiavon et al. 1997a). It is strengthened in the spectra of dwarf stars and is sensitive to the abundance of sodium (Conroy & van Dokkum 2012). The feature is a doublet in the spectra of individual stars, but the velocity dispersion in massive galaxies often blends it into a single feature.

The Wing-Ford band feature is a small absorption feature of the Iron Hydride molecule at  $0.99\mu\text{m}$  (Wing & Ford 1969). It is particularly sensitive to the lowest mass dwarf stars, weakens in  $[\text{Na}/\text{H}]$  enhanced populations and is relatively insensitive to  $\alpha$ -abundance (Conroy & van Dokkum 2012).

The Calcium Triplet is the strongest absorption feature studied in this work, and is IMF sensitive due to the fact that it is strong in giant stars but weak in dwarfs. Its use as an IMF sensitive index was studied in Cenarro et al. (2003), where an anti-correlation between the CaT equivalent width and  $\log(\sigma_0)$  was presented. Calcium is also an  $\alpha$  element, although interestingly the Ca abundance has been shown to be depressed with respect to other  $\alpha$  elements by up to

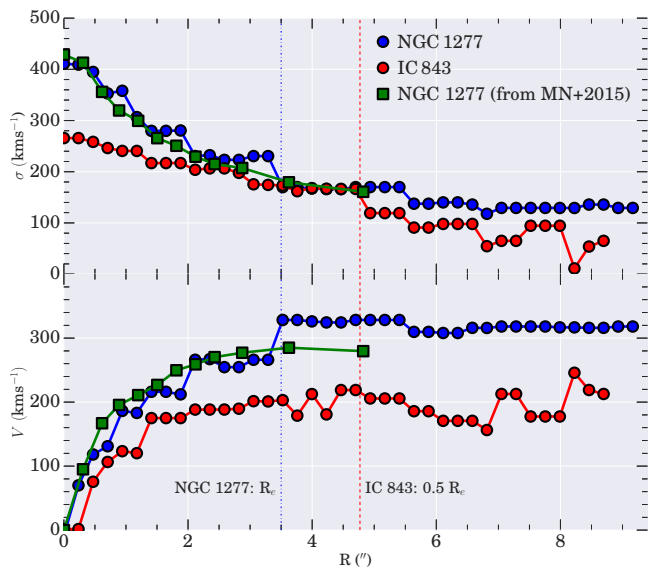


**Figure 2.** Velocity and velocity dispersion parameters for IC 843 (red) and NGC 1277 (blue). Both galaxies show large central velocity dispersions (especially NGC 1277, with  $\sigma_0=410 \text{ km s}^{-1}$ ) and ordered rotation at larger radii. Green points are long-slit observations of NGC 1277 taken from MN15.

factors of two in massive ETGs (Thomas et al. 2003). The feature also weakens in spectra with enhanced  $[\text{Na}/\text{H}]$ , and is sensitive to the  $[\text{Ca}/\text{H}]$  abundance ratio.

The TiO0.89 and MgI0.88 features are both relatively insensitive to the IMF. In the CvD12 models, the TiO bandhead is strongly sensitive to the  $\alpha$ -enhancement of the population, as well as weakening with older stellar ages. It also becomes stronger with increased  $[\text{Ti}/\text{Fe}]$  and weaker with  $[\text{C}/\text{Fe}]$ . The MgI0.88 feature displays the opposite behaviour with respect to stellar age, becoming stronger as a population ages, and becomes deeper with increasing  $[\text{Mg}/\text{Fe}]$  and  $[\alpha/\text{Fe}]$ .

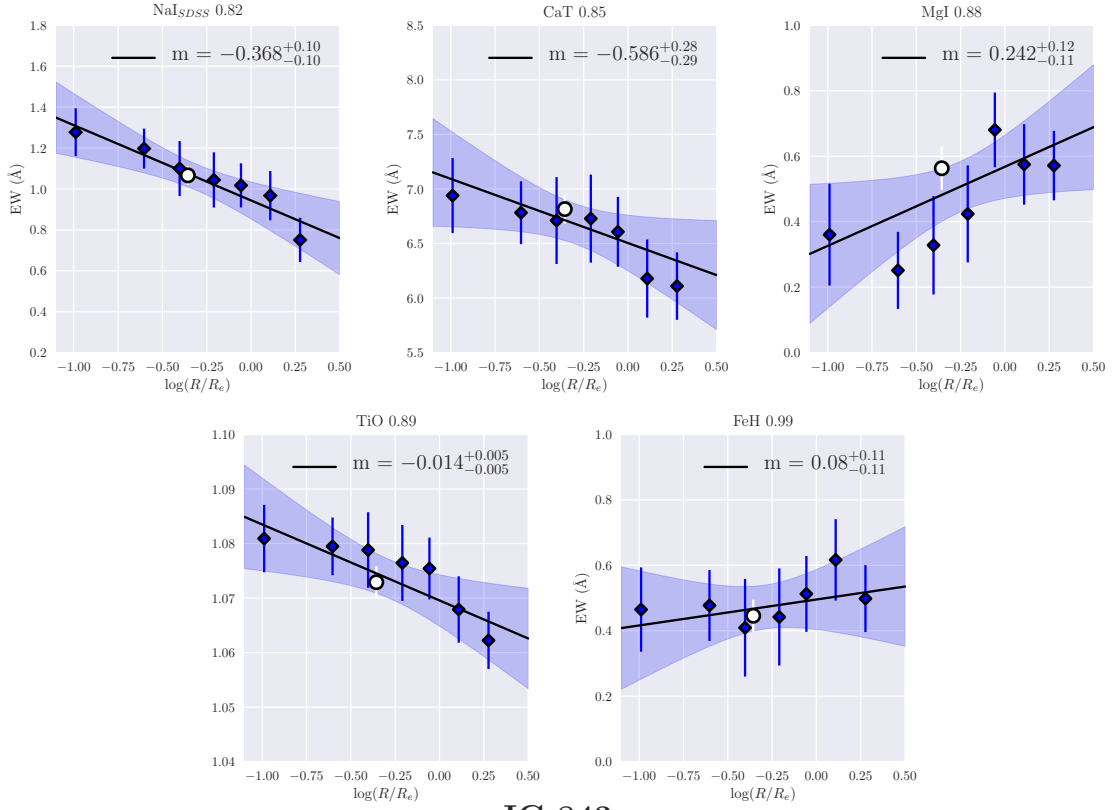
## 5 RESULTS

### 5.1 Radial variation in index strengths

Figure 3 shows the results of measuring the IMF sensitive absorption features in NGC 1277 and IC 843 as a function of radius. As discussed in Section 4, these measurements were taken at the intrinsic velocity dispersion of the radial bin and then corrected to  $200 \text{ km s}^{-1}$  for both galaxies. All results are equivalent widths, in units of  $\text{\AA}$  and found using the formalism of Cenarro et al. (2001), except for that of TiO which is a ratio of the blue and red pseudo-continua. Table 3 gives the best fitting gradient,  $m$ , of the straight line fit to each index, with  $1\sigma$  uncertainties from the marginal posterior of  $m$ .

The most significant index gradient in NGC 1277 is in NaI<sub>SDSS</sub>, which drops from an unusually large value of  $1.3 \text{\AA}$  in the very centre to  $\sim 0.8 \text{\AA}$  at  $1.9R_e$ . This behaviour is consistent with the findings of MN15, who found a similarly strong radial gradient in this object. We also measure negative gradients in the CaT (at a  $\sim 2\sigma$  significance) and the TiO0.89 ( $2.75\sigma$ ). The measurements of MgI0.88 index show a positive trend with radius, although the scatter in

## NGC 1277



## IC 843

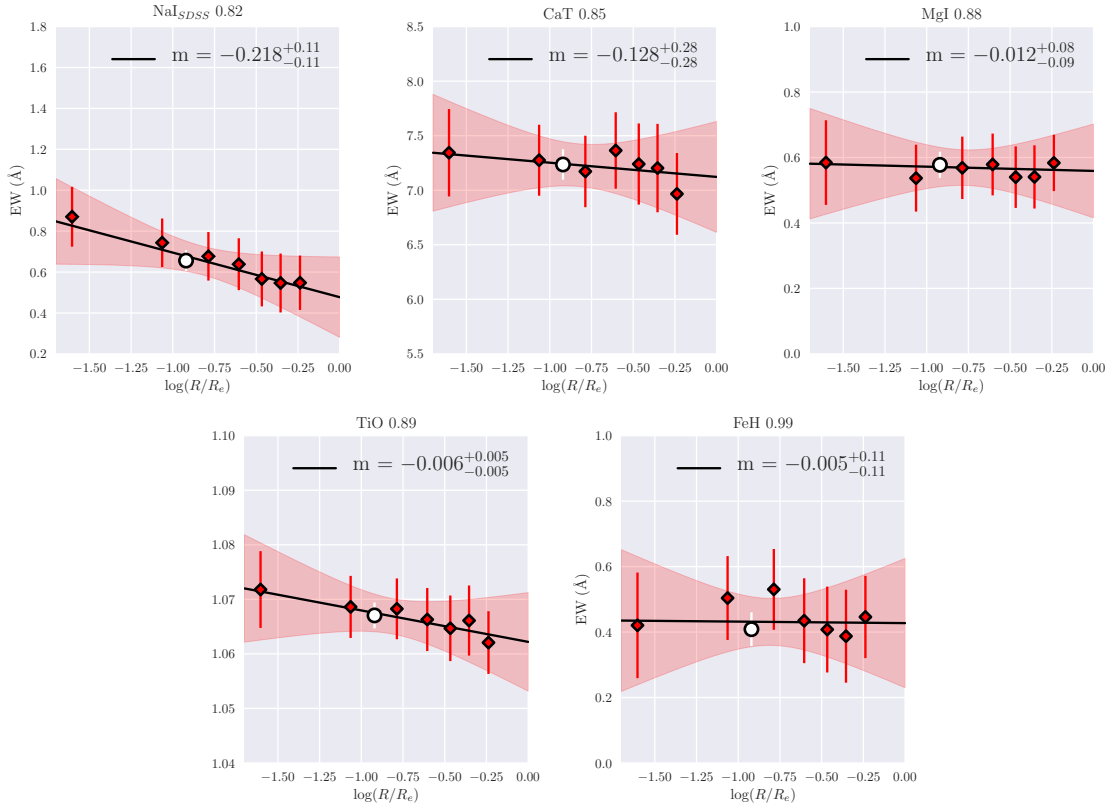


**Figure 3.** Radial measurements for each index in NGC 1277 (blue, top) and IC 843 (red, bottom). All index measurements have been corrected to a common velocity dispersion of  $200 \text{ km s}^{-1}$  (see section 4).  $1\sigma$  errors around the best fit line (encompassing uncertainty in both the gradient and intercept) are shown as shaded regions. The white circle shows the value of each index in the integrated spectrum of each galaxy.

**Table 3.** Measured index trends with respect to  $\log(R/R_e)$ , with  $1\sigma$  uncertainties. Units are  $\text{\AA}/\log(R/R_e)$ , apart from the TiO index gradient which is simply  $1/\log(R/R_e)$ .

Index	Best fit gradient	
	IC 843	NGC 1277
NaI <sub>SDSS</sub>	$-0.218^{+0.11}_{-0.11}$	$-0.368^{+0.10}_{-0.10}$
CaT	$-0.126^{+0.28}_{-0.28}$	$-0.595^{+0.29}_{-0.30}$
MgI	$-0.012^{+0.09}_{-0.09}$	$0.231^{+0.12}_{-0.12}$
TiO	$-0.006^{+0.005}_{-0.005}$	$-0.011^{+0.005}_{-0.005}$
FeH	$-0.015^{+0.11}_{-0.11}$	$0.081^{+0.11}_{-0.10}$

these measurements is large, possibly due to the effects of residual telluric absorption. We do not find evidence for a radial gradient in FeH0.99 in NGC 1277, with the gradient in index strength being consistent with zero.

The most significant gradient in IC 843 is also the NaI<sub>SDSS</sub> feature, albeit offset to a weaker index strength. We also see a significant radial trend in TiO0.89. We measure flat radial profiles for MgI0.88, the CaT and the Wing Ford band, with all three indices having a best fit gradient fully consistent with zero.

## 6 ANALYSIS

### 6.1 Stellar population synthesis models

Figure 4 shows a comparison of our NaI and FeH measurements to two sets of stellar population synthesis (SPS) models, each convolved to  $200 \text{ km s}^{-1}$  to match our measurements. The top two panels show index predictions from the CvD12 (Conroy & van Dokkum 2012) and E-MILES (Vazdekis et al. 1996) libraries for changes in IMF slope from an old (13.5 Gyr for the CvD12 models, 14.125 Gyr for E-MILES) stellar population at solar metallicity,  $\alpha$ -abundance and elemental abundance ratios. Also shown are variations in index strength with further stellar population parameters included in each set of models.

The CvD12 models allow changes in  $[\alpha/\text{Fe}]$ , age and the abundance ratios of various elements, with  $[\text{Na}/\text{Fe}]$  and  $[\text{Fe}/\text{H}]$  being most important to us here. A change in  $[\text{Fe}/\text{H}]$  of  $\pm 0.3$  dex has no effect on the predicted NaI equivalent width, whilst understandably leading to a large variation in FeH strength. The result of increasing  $[\text{Na}/\text{Fe}]$  is a strengthening of the NaI index combined with a weakening of the FeH equivalent width. This is due to the fact that Na is an important electron contributor in cool giant and dwarf stars, and large abundances of Na in these stellar atmospheres tends to encourage the dissociation of molecules like FeH. An  $\alpha$  enhanced population leads to weaker FeH and NaI predictions, especially at steeper IMF slopes, whilst the response of the FeH index to changes in population age is found to be a function of the IMF slope. A full discussion of these SPS models can be found in Conroy & van Dokkum (2012).

The E-MILES models include changes in age and metallicity. A metallicity of +0.2 dex above solar leads to increased equivalent widths for both NaI and FeH, whilst younger ages tend to weaken both indices. La Barbera et al. (2017) have produced the ‘‘Na-MILES’’ models, which are SPS templates spanning the E-MILES wavelength range with enhanced  $[\text{Na}/\text{Fe}]$  abundance ratios of up to 1.2 dex. Interestingly,

these templates predict that the FeH index is far less sensitive to the effect of  $[\text{Na}/\text{Fe}]$  enhancement than the CvD12 models.

Figure 4 also highlights a complicating factor in our interpretation of our NaI and FeH measurements: the different index predictions from the CvD12 and E-MILES models for the same value of IMF slope. The largest difference is for the most bottom heavy IMFs: the  $x = 3.5$  IMF slope prediction for FeH is  $\sim 37\%$  weaker in the E-MILES models compared to the CvD12, whilst the NaI predicted equivalent width is  $\sim 39\%$  smaller. A large part of this difference is due to the different low-mass cutoff,  $m_c$ , assumed for the IMF in each case:  $0.08 M_\odot$  in the CvD12 models and  $0.1 M_\odot$  for E-MILES. The CvD12 models therefore have a larger number of very low-mass stars and predict stronger NaI and FeH equivalent widths.

Constraining the low-mass cut off of the IMF is a technically demanding task, with recent measurements of  $m_c$  by Spiniello et al. (2015b) and Barnabè et al. (2013) combining modelling of IMF sensitive indices with constraints from strong gravitational lensing and dynamics. Since in this work we are unable to distinguish between  $m_c = 0.08 M_\odot$  and  $m_c = 0.1 M_\odot$ , we conduct our analysis and draw conclusions using both sets of SPS models.

The measurements in both galaxies scatter around similar areas of parameter space: directly above the Salpeter IMF (E-MILES models) or a point between Chabrier and Salpeter IMFs (CvD12 models) in the direction of  $[\text{Na}/\text{Fe}]$  enhancement, with the NGC 1277 points further from the model lines than IC 843. Notably, our results rule out very bottom heavy single power law IMFs with  $x > 3$  in both NGC 1277 and IC 843. Furthermore, neither galaxy is consistent with a strong gradient in a single power law IMF slope, as the measurements in both objects vary in the direction of decreasing  $[\text{Na}/\text{Fe}]$  enhancement rather than parallel to the lines of decreasing IMF slope. The simplest explanation of the position of each galaxy’s locus of points, therefore, is a constant IMF as a function of radius combined with a radial gradient in  $[\text{Na}/\text{Fe}]$ .

### 6.2 IMF determination from global measurements

Following Zieleniewski et al. (2017), we now use the global index measurements of NGC 1277 and IC 843 to make quantitative statements about the IMF slope in each galaxy. By interpolating the predicted FeH equivalent widths from the CvD12 and E-MILES models and comparing to our global FeH measurement, we measure global IMF slopes in each object. Appendix B discusses the precise calculations in detail.

One route to determine the IMF in a galaxy is to fit index strength measurements from templates to the data, minimising a  $\chi^2$ -like function for each of the index measurements from the galaxy (e.g. La Barbera et al. 2016; Martín-Navarro et al. 2015b; Alton et al. 2017). We choose not to do this here for two reasons.

Firstly, the wavelength coverage of SWIFT doesn’t allow us to measure many of the standard Lick indices which are important in constraining stellar population parameters such as age and metallicity. Furthermore, we have found that the FeH strength can be badly modelled by such a process whilst still returning an acceptable reduced  $\chi^2$  statistic. This

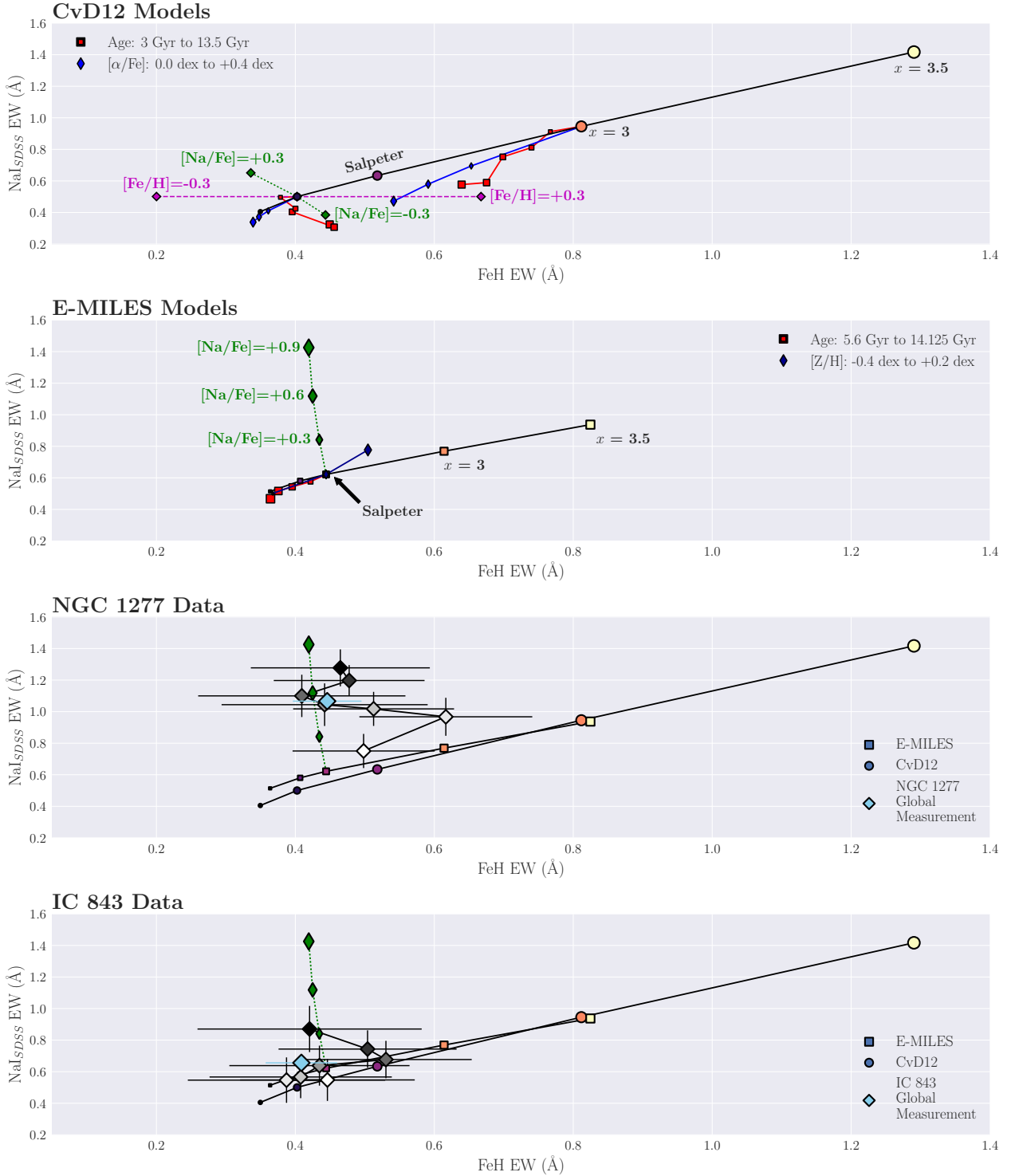


**Figure 4.** A comparison of our measurements of NaI and FeH equivalent widths to two sets of stellar population models. The upper two panels show the change in FeH and NaI equivalent width with varying stellar population parameters in the CvD12 models (first panel) and E-MILES models (second panel). The black line in both panels shows index responses to varying the IMF slope,  $x$ , in an old stellar population at solar metallicity,  $[\alpha/\text{Fe}]=0.0$  and solar elemental abundance ratios. Note the differences in index equivalent width predictions, for the same IMF slope, between the models. Changes in  $[\alpha/\text{Fe}]$  from solar to +0.4 dex (small to large blue diamonds), and age from 3 to 13.5 Gyr (large to small red squares) from a Chabrier and  $x = 3$  IMF are shown in the top panel, for the CvD12 models. Also plotted are predictions for abundance variations of  $\pm 0.3$  dex in  $[\text{Na}/\text{Fe}]$  (green) and  $[\text{Fe}/\text{H}]$  (purple) from a Chabrier IMF. The second panel shows variations of the E-MILES model predictions for ages from 5.6 to 14.125 Gyr (large to small red squares),  $[\text{Z}/\text{H}]$  from -0.4 to +0.2 dex (small to large navy diamonds) and  $[\text{Na}/\text{Fe}]$  from solar to +0.9 dex (small to large green diamonds), all from a Salpeter IMF. The lower two panels show our resolved measurements in NGC 1277 (third panel) and IC 843 (bottom panel), coloured by their radial position from the centre of the galaxy (dark) to the outskirts (light). Also shown, in light blue, are the global measurements for both galaxies. Index predictions from the models are coloured from bottom light (dark, bottom left) to bottom heavy (light, top right), with equivalent IMF slopes plotted in the same colour. In both galaxies, our measurements scatter above the predictions for Chabrier to Salpeter IMFs in the direction of  $[\text{Na}/\text{Fe}]$  enhancement. See Section 6.1 for further discussion.



is due to its small intrinsic strength, which leads to larger fractional errors on its measurement (and therefore a smaller  $\chi^2$  penalty for a bad model prediction) than other indices.

For NGC 1277, using published measurements of optical indices (which are insensitive to the IMF) from Ferré-Mateu et al. (2017) and comparing to the SPS models of Thomas et al. (2011a), we infer an age of 13.5 Gyr, a metallicity of +0.3 dex and an  $[\alpha/\text{Fe}]$  of +0.3 dex. These are in agreement with the results found by Martín-Navarro et al. (2015b), who measure NGC 1277 to be old and  $\alpha$ -enhanced at all radii with a gradient in  $[\text{Z}/\text{H}]$  from +0.4 dex in the very centre to solar at  $1.4 R_e$ .

For IC 843, we use measurements from Price et al. (2011) to find an old age of 10 Gyr, an  $[\alpha/\text{Fe}]$  enhancement of +0.3 dex and a  $[\text{Z}/\text{H}]$  of +0.2 dex.

As Figure 4 shows, the FeH index is sensitive to  $[\text{Na}/\text{Fe}]$  abundance. Using the global measurement as a guide, the Na-MILES models imply enhancements in  $[\text{Na}/\text{Fe}]$  of  $\sim+0.5$  dex in NGC 1277 and  $\sim+0.1$  dex in IC 843 respectively.

Figure 5 shows the derived single-power law IMF slope for IC 843 and NGC 1277, plotted against their central velocity dispersion. A full discussion of this calculation is presented in Appendix B. Diamonds show the IMF slopes derived using the CvD12 stellar population models, whilst triangles show those found using the E-MILES models.

To measure the effect of uncertainty in the assumed stellar population parameters for each galaxy, we modelled each parameter as a normal distribution centred on the values described above and with a width of 0.1 dex for  $[\text{Z}/\text{H}]$ ,  $[\text{Fe}/\text{H}]$ ,  $[\text{Na}/\text{H}]$  and  $[\alpha/\text{Fe}]$  and a width of 1 Gyr for the age. We drew 1000 random samples from the distribution of each parameter, then recalculated the IMF slope in each case. The 16th and 84th percentiles of these samples are plotted as the blue shaded regions in Figure 5.

As shown are measurements from Zieleniewski et al. (2017), as well as the proposed correlations between unimodal IMF slope and  $\sigma_0$  from Ferreras et al. (2013), La Barbera et al. (2013b) and Spiniello et al. (2014). Both galaxies are consistent with a Salpeter IMF slope if the low-mass cut-off is  $0.08 M_\odot$  (i.e if the CvD12 models are used) or slightly above Salpeter ( $2.55 \pm 0.2$  for NGC 1277 and  $2.76 \pm 0.2$  for IC 843) if the low mass cut-off is  $0.1 M_\odot$  and we use the E-MILES models.

### 6.3 M/L values

Using these global IMF measurements, we derive V-band stellar mass-to-light values for these galaxies. For NGC 1277, we find  $(M/L)_V = 6.69^{+2.6}_{-1.7}$  using the CvD12 models and  $(M/L)_V = 10.26^{+4.3}_{-2.4}$  using the E-MILES models. For IC 843, we find  $(M/L)_V = 6.03^{+3.7}_{-2.0}$  using CvD12 and  $(M/L)_V = 9.32^{+6.2}_{-3.1}$  using E-MILES.

The values from the E-MILES models are systematically higher than those from the CvD12 models, as expected since the E-MILES IMF determinations are also more bottom heavy. The values from both sets of models are still marginally consistent within the error bars for both galaxies, however. They are also in good agreement with dynamical observations of these objects. Using adaptive optics spectroscopy, Walsh et al. (2016) find  $(M/L)_V = 9.3 \pm 1.6$  in the very centre of NGC 1277, whilst seeing limited obser-

vations out to  $\sim 3R_e$  (a similar radius to our observations) by Yıldırım et al. (2015) find  $(M/L)_V = 6.5 \pm 1.5$ , under the assumption of a constant stellar  $(M/L)$  with radius.

MN15 infer the V-band stellar  $(M/L)_V$  ratio in NGC 1277 to be 7.5 at  $1.4 R_e$ , rising to 11.6 in the centre, from their analysis of IMF-sensitive absorption features and the assumption of a bimodal IMF. Whilst we are unable to make such a resolved  $(M/L)_V$  measurement with our data, these values are generally in agreement with our integrated measurement (which extends out to just over  $2.2 R_e$ ).

In IC 843, Thomas et al. (2007) make a dynamical measurement of the  $(M/L)$  in the  $R_c$  band, with observations extending to further than  $3R_e$ . They find  $(M/L)_{R_c} = 10.0$  and conclude that mass follows light in this object. Our inferred IMFs (from an integrated spectrum out to  $0.65 R_e$ ), combined with published age and metallicity measurements, lead to  $(M/L)_{R_c} = 7.504^{+4.74}_{-2.43}$  using the E-MILES models and  $4.933^{+3.01}_{-1.64}$  using the CvD12 models. These are both lower than the value from Thomas et al., although consistent within the error bars for the E-MILES models. This may be evidence, therefore, for a dark matter profile in this object which closely follows the visible matter.

## 7 DISCUSSION

The main result of this work is the strong gradient in NaI0.82 absorption combined with flat profiles for FeH0.99 in both objects. The equivalent widths of FeH in both galaxies also scatter around a similar value:  $0.4 \text{ \AA}$  at a velocity dispersion of  $200 \text{ km s}^{-1}$ .

This behaviour may seem surprising, since both FeH and NaI indices are found to be IMF sensitive: i.e. vary their strength between dwarf and giant stars of the same spectral type. Whilst it is true that the Wing-Ford band and NaI are both caused by absorption in the atmospheres of dwarf stars, each is strongest in stars of a slightly different mass. In the case of an old, evolved, stellar population, FeH is more sensitive than NaI to stars below around  $0.2 M_\odot$  whereas NaI is stronger at  $0.2 M_\odot < M < 0.6 M_\odot$  (Conroy & van Dokkum 2012, Figure 17).

The simplest explanation for our flat FeH measurements at  $0.4 \text{ \AA}$  are that the quantity that the Wing-Ford band is sensitive to is not changing, either within or between these galaxies. A scenario in which two separate quantities which affect the FeH absorption feature vary in opposite directions to each other is possible, but given that our measurements in these two object are qualitatively similar to the findings of Zieleniewski et al. (2015), McConnell et al. (2016), Zieleniewski et al. (2017), Alton et al. (2017) and others (see section 7.1 for further discussion) we find such a conspiracy unlikely.

If we make the simple assumption that the IMF takes a unimodal form below  $1 M_\odot$ , we can use the lack of change of the FeH absorption features to rule out a large radial gradient in the IMF in both NGC 1277 and IC 843. Under this assumption, we can also attribute the radial change in the NaI0.82 index to a gradient in the abundance of  $[\text{Na}/\text{Fe}]$  in both galaxies, with the central enhancement in  $[\text{Na}/\text{Fe}]$  being smaller in IC 843 than NGC 1277.

Such gradients in  $[\text{Na}/\text{Fe}]$  within individual galaxies have been recently been measured in the context of IMF vari-

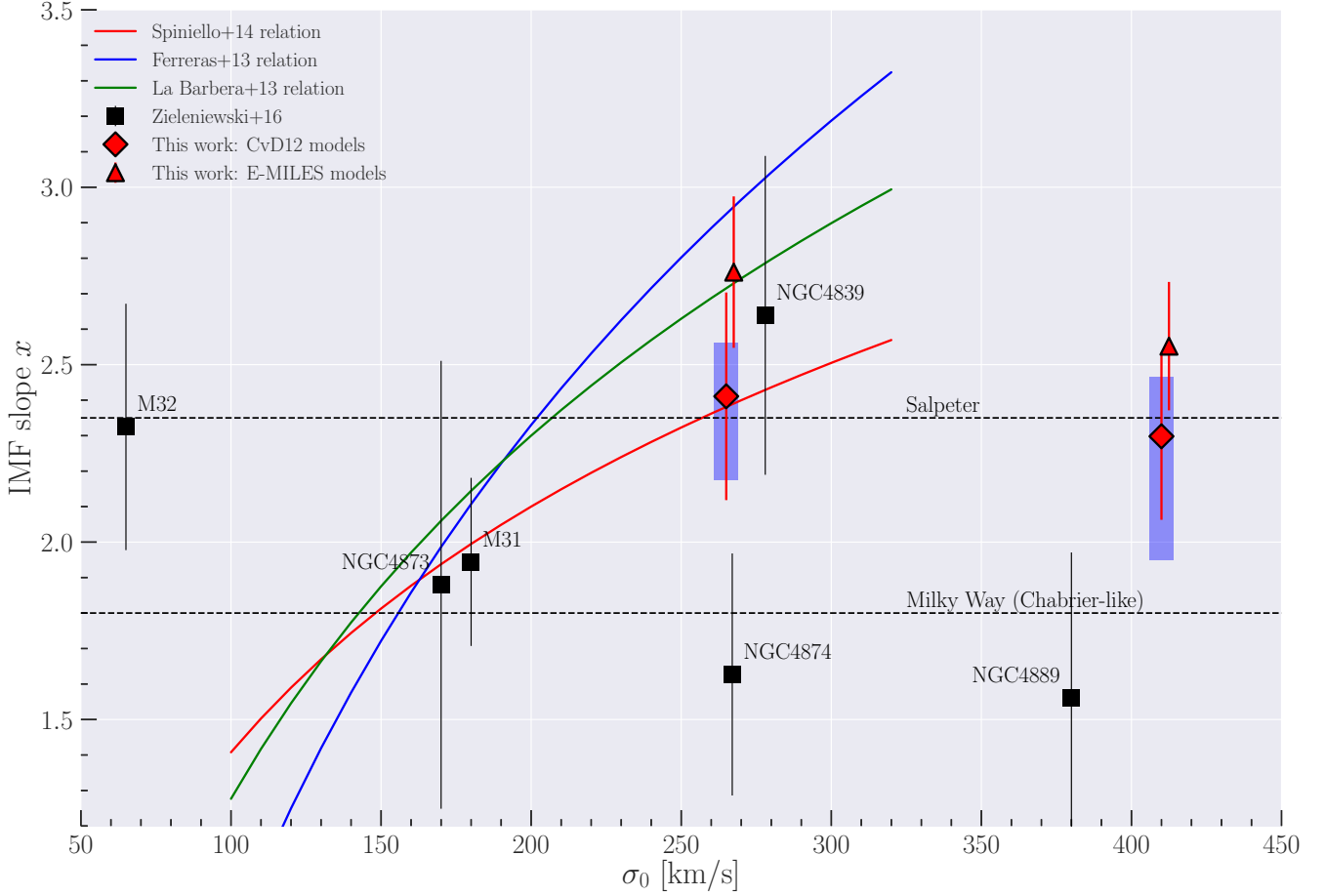


**Figure 5.** Derived IMF slope for both galaxies studied in this work, plotted against their central velocity dispersion. Discussion of the IMF slope calculation is presented in Appendix B. Diamonds correspond to the values derived using the CvD12 stellar population models and triangles denote the values found using the E-MILES models (which are slightly offset in the  $x$  direction). See section 6.2 for details. Red error bars denote measurement uncertainties. The blue shaded regions show the effect of uncertainties in the stellar population parameters assumed for each galaxy. They are derived by assigning a normal distribution to each parameter (centred on the appropriate values and of width 0.1 dex for  $[Z/H]$ ,  $[Fe/H]$ ,  $[Na/H]$  and  $[\alpha/Fe]$ , 1 Gyr for age), then drawing 1000 samples and calculating the IMF for each one. The blue regions denote the 16th and 84th percentiles of these samples. A similarly sized uncertainty in the population parameters also applies to the E-MILES model points, but is not shown for clarity. Coloured lines show proposed unimodal IMF- $\sigma_0$  correlations from Ferreras et al. (2013), La Barbera et al. (2013b) and Spiniello et al. (2014), whilst black squares are values from Zieleniewski et al. (2017). Note that measurements from Zieleniewski et al. (2017) utilise the CvD12 models.

ations. van Dokkum et al. (2016) used long-slit spectroscopy and full-spectral fitting to measure abundance gradients in six nearby ETGs as well as gradients in the IMF. Alton et al. (2017) also measure a gradient in  $[Na/Fe]$  in a stack of 8 nearby ETGs, finding  $\Delta[Na/Fe] = -0.35$  dex per decade in  $\log(R/R_e)$ . Similar abundance gradients were measured for those individual galaxies in the stack with high enough quality data. Interestingly, unlike van Dokkum et al. (2016), they find no evidence for IMF gradients in their data, with the IMF in their stacked spectrum being uniformly Salpeter throughout.

Super solar  $[Na/Fe]$  abundance ratios are also not uncommon in massive ETGs. Jeong et al. (2013) find excess NaD line strengths in  $\sim 8\%$  of low redshift ( $z < 0.08$ ) SDSS DR7 galaxies, including in ETGs without visible dust lanes, and conclude that  $[Na/Fe]$  enhancement, rather than ISM or IMF effects, are the cause. Furthermore, both Worthey et al. (2014) and Conroy et al. (2014) find a trend of in-

creasing  $[Na/Fe]$  abundance in galaxies with larger velocity dispersions, of up to  $\sim 0.4$  dex in galaxies with  $\sigma = 300 \text{ km s}^{-1}$ , using independent SPS models.

The interpretation of our results in favour of an abundance gradient in  $[Na/Fe]$  relies on our understanding of the strength of the Wing-Ford band being correct: could a positive abundance gradient in  $[Fe/H]$  be suppressing the FeH absorption strength in the centre and masking a bottom heavy IMF? Possible iron abundance variations can be easily constrained by optical indices such as Fe52 and/or Fe53 (Conroy & van Dokkum 2012), and optical measurements from Ferré-Mateu et al. (2017) and Price et al. (2011) show no evidence for a low  $[Fe/H]$  ratio in either NGC 1277 or IC 843. The production and abundance ratios of iron and hydrogen have been well studied and understood for decades (e.g. Faber 1983; Davies et al. 1993; Worthey et al. 1994; Trager et al. 1998), and measuring an  $[Fe/H]$  under-abundance of  $\sim 0.3$  dex in either of these mas-

sive ETGs would be surprising. FeH is also relatively insensitive to  $[\alpha/\text{Fe}]$  enhancement and age gradients (Conroy & van Dokkum 2012).

A second, independent explanation of our measurements would be that the IMF varies radially but does not have the shape of a single power law. In the “bimodal” parameterisation of Vazdekis et al. (1996), the IMF is flat at masses below  $0.2 M_{\odot}$  whilst the high mass slope (above  $0.6 M_{\odot}$ ) varies. The region in between is connected by spline interpolation. MN15 use this bimodal IMF parameterisation in their study of NGC 1277. They found evidence for a bottom heavy bimodal IMF of  $\Gamma_b = 3$  out to  $0.3 R_e$ , which decreases and flattens off to  $\Gamma_b = 2.5$  between  $0.8 R_e$  and  $1.4 R_e$ . Such an IMF shape introduces a degeneracy between the FeH and NaI indices, by decoupling the very low-mass end of the IMF from the region between  $0.2 M_{\odot} < M < 0.6 M_{\odot}$ . Qualitatively, this allows a change in NaI strength without the corresponding change in FeH.

Variations in the high-mass slope of the IMF from the Salpeter value of 2.35, such as in the case of a bottom-heavy bimodal IMF, can be constrained by a number of observations. Since the high mass slope of the IMF sets the ratio of massive stars ( $M > 8 M_{\odot}$ ) to stars of around  $M_{\odot}$ , the low-mass X-ray binary populations of nearby ellipticals depend on the slope of the IMF. Peacock et al. (2014) use this fact to constrain the high-mass IMF slope in 8 nearby ellipticals, finding results consistent with an invariant high mass slope in these objects (rather than varying as a function of  $\sigma$ ).

Furthermore, the fundamental plane (FP) of elliptical galaxies (the plane in the space of central velocity dispersion, effective radius and effective surface brightness) should depend on the slope of the IMF above the main sequence turn off, roughly  $1 M_{\odot}$ . A stellar population with a very flat high mass IMF slope will decline in luminosity quickly after a burst of star formation, whereas the decline for a population with an abundance of low-mass stars will proceed more slowly. As described in Renzini (2005), if the IMF above  $1 M_{\odot}$  varied from galaxy to galaxy this effect would lead to a rotation of the FP with redshift, since elliptical galaxies with a flatter high-mass IMF slope would depart from the FP by a different amount to those ellipticals with a steeper high-mass slope. Studies of the FP of galaxy clusters from  $z \sim 0.5$  to  $z \sim 1$  (e.g. Wuyts et al. 2004; Holden et al. 2010; Oldham et al. 2017) do not show a departure from the slope measured in clusters in the local universe.

van Dokkum & Conroy (2012) also use a parameterisation of the IMF which is not a single power law. Their IMF is fixed at high masses (above  $1 M_{\odot}$ ) and is a two part power law below, with a break at  $0.5 M_{\odot}$ . This form of the low-mass IMF would allow the NaI and FeH indices to vary independently of each other too, and could explain their behaviour in NGC 1277 and IC 843.

With the data available to us, we are unable to rule out the possibility that our divergent NaI and FeH measurements are caused by a more complicated form of the IMF than a simple power law. A wavelength range covering further spectral indices, such as the Na D index and various optical Fe lines, combined with the publicly available state of the art stellar population models, would allow us to make concrete statements about both the IMF and population parameters in these objects.

## 7.1 Other radial studies of FeH and NaI indices

Similar results and conclusions to ours have been reached by other authors who have measured both NaI and FeH indices as a function of radius in a variety of objects. As mentioned perviously, Alton et al. (2017) find a strong gradient in NaI and radially flat FeH in a stack of 8 massive ETGs. They conclude a bottom heavy IMF at all radii. Zieleniewski et al. (2015) studied the central bulge of M31, observing a large decrease in NaI combined with no radial change in FeH, and conclude in favour of a gradient in  $[\text{Na}/\text{Fe}]$  rather than the IMF. Furthermore, Zieleniewski et al. (2017) studied the brightest cluster galaxies (BCGs) in the Coma cluster, measuring a strong gradient in NaI combined with flat FeH profile in the massive ETG NGC 4889, which has a central velocity dispersion of nearly  $400 \text{ km s}^{-1}$ . Other objects in the sample also show weak FeH absorption. Only NGC 4839 displays evidence for a deep Wing-Ford band, although large systematic uncertainty due to residual sky emission prevents the authors from drawing strong conclusions about its stellar population.

McConnell et al. (2016) obtained deep long-slit data on two nearby ETGs, both of which had been part of the van Dokkum & Conroy (2012) sample. They found strong gradients in NaI but a much weaker decline in FeH, as well as opposite behaviour in  $\text{NaI}/\langle\text{Fe}\rangle$  and  $\text{FeH}/\langle\text{Fe}\rangle$ . Again, the authors conclude in favour of a variation in  $[\text{Na}/\text{Fe}]$  over the central  $\sim 300 \text{ pc}$  of each galaxy instead of the IMF driving the strong decline in NaI. The authors also argue, as we do, that the flat FeH profile implies a fixed low-mass slope of the IMF below  $M < \sim 0.4 M_{\odot}$ .

Finally, La Barbera et al. (2016, 2017) make resolved measurements of the Wing-Ford band and a number of Na indices to constrain the shape of the low-mass IMF in a nearby ETG. They too find a lack of radial variation in FeH combined with negative gradients in NaI, NaD and two further Na lines at  $1.14$  and  $2.21 \mu\text{m}$ , from which they conclude a gradient in a bimodal IMF combined with a  $[\text{Na}/\text{Fe}]$  gradient.

As well as displaying the same qualitative behaviour to this work, most of the studies mentioned above also find FeH equivalent widths of similar values to those presented here:  $0.3\text{-}0.4 \text{ \AA}$ , at a velocity dispersion of around  $200 \text{ km s}^{-1}$ . The slight exceptions are the measurements of Alton et al. (2017), which are slightly lower than this at  $0.2\text{-}0.3 \text{ \AA}$  at a velocity dispersion of  $230 \text{ km s}^{-1}$ , and La Barbera et al. (2016, 2017), who measure the FeH equivalent width to be  $0.5\text{-}0.45 \text{ \AA}$  at a velocity dispersion of  $300 \text{ km s}^{-1}$ . This means that, as well as numerous studies finding little to no radial variation of FeH within galaxies, the FeH index has a generally consistent value between galaxies too.

## 8 CONCLUSIONS

We have used the Oxford SWIFT instrument to undertake a study of two low redshift early-type galaxies in order to make resolved measurements IMF sensitive indices in their spectra. We obtained high S/N integral field data of NGC 1277, a fast rotator in the Perseus cluster with a very high central velocity dispersion, and IC 843, also a fast rotator, located in the Coma cluster. Our measurements extend out to

7.7'' and 6.2'' respectively, corresponding to 2.2 and 0.65  $R_e$ . The SWIFT wavelength coverage, from 6300 Å to 10412 Å, allows radial measurement of the NaI doublet, CaII triplet, TiO, MgI and FeH spectral features. We conclude:

(i) NGC 1277 shows a strong negative gradient in NaI, more marginal negative TiO and CaT gradients and a flat FeH profile. The FeH equivalent widths scatter around 0.42 Å at all radii (corrected to 200 km $s^{-1}$ ).

(ii) IC 843 is similar, if less extreme, than NGC 1277. It displays a weaker NaI and TiO gradients, and flat profiles in FeH, CaT and MgI. FeH equivalent widths are a similar strength to NGC 1277, also around 0.4 Å.

(iii) Similarly to [McConnell et al. \(2016\)](#), [Zieleniewski et al. \(2017\)](#), [Alton et al. \(2017\)](#) and others, we find very different radial trends between the IMF sensitive indices NaI and FeH.

(iv) In both NGC 1277 and IC 843, if we make the simple assumption that the IMF is a single power law below 1  $M_\odot$ , we can rule out a large IMF gradient and attribute the radial change in NaI absorption to a gradient in [Na/Fe]. Our data do not allow us to investigate more complicated IMF parameterisations (such as the one used in M15) and so we cannot rule out a gradient in a “bimodal” or multi-segment IMF.

(v) We use our global FeH measurements with state-of-the-art stellar population models to infer global single power-law IMFs in each object. Using the CvD12 models (which assume a low-mass cut-off of 0.08  $M_\odot$  for the IMF), we find IMF slopes consistent with Salpeter in each object. Using the E-MILES models (which assume a low-mass cut-off of 0.1  $M_\odot$ ), the inferred IMFs are steeper than Salpeter for both galaxies. Our inferred V band stellar mass-to-light ratios are in agreement with published dynamical and spectroscopic determinations. In IC 843, we find a mass-to-light ratio ( $R_c$  band) smaller than the dynamical ( $M/L$ ) from [Thomas et al. \(2007\)](#), despite their conclusion that mass follows light in this galaxy. If true, this implies a non-standard dark matter profile in this object.

## ACKNOWLEDGEMENTS

We would like to thank F. La Barbera for a referee report which greatly improved this work, as well as for making available the Na-MILES models used in this paper. SPV would like to thank P. Alton for fruitful discussions on the effect of Na on stellar atmospheres, and A. Ferré-Mateu for making her optical measurements of NGC 1277 available.

This paper made use of the Astropy python package ([Astropy Collaboration et al. 2013](#)), as well as the `matplotlib` ([Hunter 2007](#)) and `seaborn` plotting software ([Waskom et al. 2015](#)) and the scientific libraries `numpy` ([Van Der Walt et al. 2011](#)) and `scipy` ([Jones et al. 2001](#)).

The Oxford SWIFT integral field spectrograph was supported by a Marie Curie Excellence Grant from the European Commission (MEXT-CT-2003-002792, Team Leader: N. Thatte). It was also supported by additional funds from the University of Oxford Physics Department and the John Fell OUP Research Fund. Additional funds to host and support SWIFT at the 200-inch Hale Telescope on Palomar were provided by Caltech Optical Observatories.

This work was supported by the Astrophysics at

Oxford grants (ST/H002456/1 and ST/K00106X/1) as well as visitors grant (ST/H504862/1) from the UK Science and Technology Facilities Council. SPV is supported by a doctoral studentship supported by STFC grant ST/N504233/1. RCWH was supported by the Science and Technology Facilities Council (STFC grant numbers ST/H002456/1, ST/K00106X/1 & ST/J002216/1). RLD acknowledges travel and computer grants from Christ Church, Oxford, and support from the Oxford Centre for Astrophysical Surveys, which is funded through generous support from the Hintze Family Charitable Foundation.

## References

- Alton P. D., Smith R. J., Lucey J. R., 2017, *MNRAS*, **468**, 1594  
 Anderson T. W., Darling D. A., 1954, *Journal of the American Statistical Association*, **49**, 765  
 Astropy Collaboration et al., 2013, *A&A*, **558**, A33  
 Barnabè M., Spiniello C., Koopmans L. V. E., Trager S. C., Czoske O., Treu T., 2013, *MNRAS*, **436**, 253  
 Bastian N., Covey K. R., Meyer M. R., 2010, *ARA&A*, **48**, 339  
 Cappellari M., Emsellem E., 2004, Publications of the Astronomical Society of the Pacific, **116**, 138  
 Cappellari M., et al., 2011, *MNRAS*, **413**, 813  
 Cappellari M., et al., 2013, *MNRAS*, **432**, 1862  
 Cenarro A. J., Cardiel N., Gorgas J., Peletier R. F., Vazdekis A., Prada F., 2001, *MNRAS*, **326**, 959  
 Cenarro A. J., Gorgas J., Vazdekis A., Cardiel N., Peletier R. F., 2003, *MNRAS*, **339**, L12  
 Chabrier G., 2003, *PASP*, **115**, 763  
 Clauwens B., Schaye J., Franx M., 2016, *MNRAS*, **462**, 2832  
 Clough S. A., Shephard M. W., Mlawer E. J., Delamere J. S., Iacono M. J., Cady-Pereira K., Boukabara S., Brown P. D., 2005, *J. Quant. Spectrosc. Radiative Transfer*, **91**, 233  
 Cohen J. G., 1978, *ApJ*, **221**, 788  
 Conroy C., van Dokkum P., 2012, *ApJ*, **747**, 69  
 Conroy C., Graves G. J., van Dokkum P. G., 2014, *ApJ*, **780**, 33  
 Couture J., Hardy E., 1993, *ApJ*, **406**, 142  
 Davies R. I., 2007, *MNRAS*, **375**, 1099  
 Davies R. L., Sadler E. M., Peletier R. F., 1993, *MNRAS*, **262**, 650  
 Emsellem E., 2013, *MNRAS*, **433**, 1862  
 Faber S. M., 1983, *Highlights of Astronomy*, **6**, 165  
 Faber S. M., French H. B., 1980, *Lick Observatory Bulletin*, **823**, 1  
 Ferré-Mateu A., Trujillo I., Martín-Navarro I., Vazdekis A., Mezcua M., Balcells M., Domínguez L., 2017, *MNRAS*,  
 Ferreras I., La Barbera F., de la Rosa I. G., Vazdekis A., de Carvalho R. R., Falcón-Barroso J., Ricciardelli E., 2013, *MNRAS*, **429**, L15  
 Holden B. P., van der Wel A., Kelson D. D., Franx M., Illingworth G. D., 2010, *ApJ*, **724**, 714  
 Hopkins P. F., Bundy K., Murray N., Quataert E., Lauer T. R., Ma C.-P., 2009, *MNRAS*, **398**, 898  
 Hunter J. D., 2007, *Computing In Science & Engineering*, **9**, 90  
 Jeong H., Yi S. K., Kyeong J., Sarzi M., Sung E.-C., Oh K., 2013, *ApJS*, **208**, 7  
 Jones E., Oliphant T., Peterson P., et al., 2001, SciPy: Open source scientific tools for Python, <http://www.scipy.org/>  
 Kausch W., et al., 2014, in Manset N., Forshay P., eds, *Astronomical Society of the Pacific Conference Series Vol. 485, Astronomical Data Analysis Software and Systems XXIII*. p. 403 ([arXiv:1401.7768](https://arxiv.org/abs/1401.7768))  
 Kroupa P., 2001, *MNRAS*, **322**, 231  
 La Barbera F., Ferreras I., Vazdekis A., de la Rosa I. G., de

Carvalho R. R., Trevisan M., Falcón-Barroso J., Ricciardelli E., 2013a, *MNRAS*, **433**, 3017

La Barbera F., Ferreras I., Vazdekis A., de la Rosa I. G., de Carvalho R. R., Trevisan M., Falcón-Barroso J., Ricciardelli E., 2013b, *MNRAS*, **433**, 3017

La Barbera F., Vazdekis A., Ferreras I., Pasquali A., Cappellari M., Martín-Navarro I., Schönebeck F., Falcón-Barroso J., 2016, *MNRAS*, **457**, 1468

La Barbera F., Vazdekis A., Ferreras I., Pasquali A., Allende Prieto C., Röck B., Aguado D. S., Peletier R. F., 2017, *MNRAS*, **464**, 3597

Martín-Navarro I., Barbera F. L., Vazdekis A., Falcón-Barroso J., Ferreras I., 2015a, *MNRAS*, **447**, 1033

Martín-Navarro I., La Barbera F., Vazdekis A., Ferré-Mateu A., Trujillo I., Beasley M. A., 2015b, *MNRAS*, **451**, 1081

Martín-Navarro I., et al., 2015c, *ApJ*, **806**, L31

McConnell N. J., Lu J. R., Mann A. W., 2016, *ApJ*, **821**, 39

Naab T., Johansson P. H., Ostriker J. P., 2009, *ApJ*, **699**, L178

Oldham L. J., Houghton R. C. W., Davies R. L., 2017, *MNRAS*, **465**, 2101

Peacock M. B., Zepf S. E., Maccarone T. J., Kundu A., Gonzalez A. H., Lehmer B. D., Maraston C., 2014, *ApJ*, **784**, 162

Price J., Phillips S., Huxor A., Smith R. J., Lucey J. R., 2011, *MNRAS*, **411**, 2558

Renzini A., 2005, in Corbelli E., Palla F., Zinnecker H., eds, *Astrophysics and Space Science Library Vol. 327, The Initial Mass Function 50 Years Later*. p. 221 ([arXiv:astro-ph/0410295](https://arxiv.org/abs/astro-ph/0410295)), [doi:10.1007/978-1-4020-3407-7\\_43](https://doi.org/10.1007/978-1-4020-3407-7_43)

Salpeter E. E., 1955, *ApJ*, **121**, 161

Schiavon R. P., Barbuy B., Rossi S. C. F., Milone A. 1997a, *ApJ*, **479**, 902

Schiavon R. P., Barbuy B., Singh P. D., 1997b, *ApJ*, **484**, 499

Smith R. J., 2014, *MNRAS*, **443**, L69

Smith R. J., Lucey J. R., Conroy C., 2015, *MNRAS*, **449**, 3441

Spiniello C., Trager S., Koopmans L. V. E., Conroy C., 2014, *MNRAS*, **438**, 1483

Spiniello C., Barnabè M., Koopmans L. V. E., Trager S. C., 2015a, *MNRAS*, **452**, L21

Spiniello C., Barnabè M., Koopmans L. V. E., Trager S. C., 2015b, *MNRAS*, **452**, L21

Spinrad H., Taylor B. J., 1971, *ApJS*, **22**, 445

Thatte N., Tecza M., Clarke F., Goodsall T., Lynn J., Freeman D., Davies R. L., 2006, in *Society of Photo-Optical Instrumentation Engineers (SPIE) Conference Series*. p. 62693L, [doi:10.1117/12.670859](https://doi.org/10.1117/12.670859)

Thomas D., Maraston C., Bender R., 2003, *MNRAS*, **343**, 279

Thomas J., Saglia R. P., Bender R., Thomas D., Gebhardt K., Magorrian J., Corsini E. M., Wegner G., 2007, *MNRAS*, **382**, 657

Thomas D., Maraston C., Johansson J., 2011a, *MNRAS*, **412**, 2183

Thomas J., et al., 2011b, *MNRAS*, **415**, 545

Trager S. C., Worthey G., Faber S. M., Burstein D., González J. J., 1998, *ApJS*, **116**, 1

Trager S. C., Faber S. M., Worthey G., González J. J., 2000, *AJ*, **120**, 165

Treu T., Auger M. W., Koopmans L. V. E., Gavazzi R., Marshall P. J., Bolton A. S., 2010, *ApJ*, **709**, 1195

Trujillo I., Ferré-Mateu A., Balcells M., Vazdekis A., Sánchez-Blázquez P., 2014, *ApJ*, **780**, L20

Van Der Walt S., Colbert S. C., Varoquaux G., 2011, preprint, ([arXiv:1102.1523](https://arxiv.org/abs/1102.1523))

Vazdekis A., Casuso E., Peletier R. F., Beckman J. E., 1996, *ApJS*, **106**, 307

Walsh J. L., van den Bosch R. C. E., Gebhardt K., Yıldırım A., Richstone D. O., Gültekin K., Husemann B., 2016, *ApJ*, **817**, 2

Waskom M., et al., 2015, seaborn: v0.6.0 (June 2015),

[doi:10.5281/zenodo.19108](https://doi.org/10.5281/zenodo.19108), <https://doi.org/10.5281/zenodo.19108>

Weijmans A.-M., et al., 2009, *MNRAS*, **398**, 561

Wing R. F., Ford Jr. W. K., 1969, *PASP*, **81**, 527

Worthey G., Faber S. M., Gonzalez J. J., Burstein D., 1994, *ApJS*, **94**, 687

Worthey G., Tang B., Serven J., 2014, *ApJ*, **783**, 20

Wuyts S., van Dokkum P. G., Kelson D. D., Franx M., Illingworth G. D., 2004, *ApJ*, **605**, 677

Yıldırım A., van den Bosch R. C. E., van de Ven G., Husemann B., Lyubenova M., Walsh J. L., Gebhardt K., Gültekin K., 2015, *MNRAS*, **452**, 1792

Zieleniewski S., Houghton R. C. W., Thatte N., Davies R. L., 2015, *MNRAS*, **452**, 597

Zieleniewski S., Houghton R. C. W., Thatte N., Davies R. L., Vaughan S. P., 2017, *MNRAS*, **465**, 192

van Dokkum P. G., 2001, *PASP*, **113**, 1420

van Dokkum P. G., Conroy C., 2010, *Nature*, **468**, 940

van Dokkum P. G., Conroy C., 2012, *ApJ*, **760**, 70

van Dokkum P., Conroy C., Villaume A., Brodie J., Romanowsky A., 2016, preprint, ([arXiv:1611.09859](https://arxiv.org/abs/1611.09859))

van den Bosch R. C. E., Gebhardt K., Gültekin K., van de Ven G., van der Wel A., Walsh J. L., 2012, *Nature*, **491**, 729

## APPENDIX A: SKY SUBTRACTION METHODS

### A1 Sky subtraction with pPXF

First order sky subtraction was applied to each galaxy cube. This involved subtracting a separate “sky” cube, made by combining sky observations taken throughout the night, from the combined galaxy data. Since night sky emission lines vary with a timescale of order minutes, similar in length to our observations, such a first order sky subtraction will not be perfect and the resulting sky subtracted spectra still contain residual sky light. To subtract this residual sky emission, we use pPXF to fit a set of sky templates at the same time as measuring the kinematics from each spectrum, a process first described in Weijmans et al. (2009).

The sky templates are made from the sky cube used for first order sky subtraction. The observed sky spectrum is split around selected molecular bandheads and transitions, according to wavelengths defined in Davies (2007), so that emission lines corresponding to different molecules are allowed to be scaled separately in pPXF. A small number of further splits were introduced by finding where sky residuals were seen to sharply change sign. We also allow for over-subtracted skylines by including negatively scaled sky spectra. A full sky spectrum with locations of sky splits marked is shown in Figures A1 and A2.

The area worst affected by residual sky emission is the Wing-Ford band at 9916 Å. Here, we found that changing the combination of sky splits had an impact on the quality of sky subtraction, and hence on the FeH equivalent width measurement. To quantitatively choose the set of skyline splits which gave us the best sky subtraction, we investigated the residuals of the sky subtracted spectrum around the best fitting pPXF template. These residuals will generally be distributed like a Gaussian around zero, with any remaining skyline residuals appearing as large positive or negative outliers. A set of residuals which have tails which

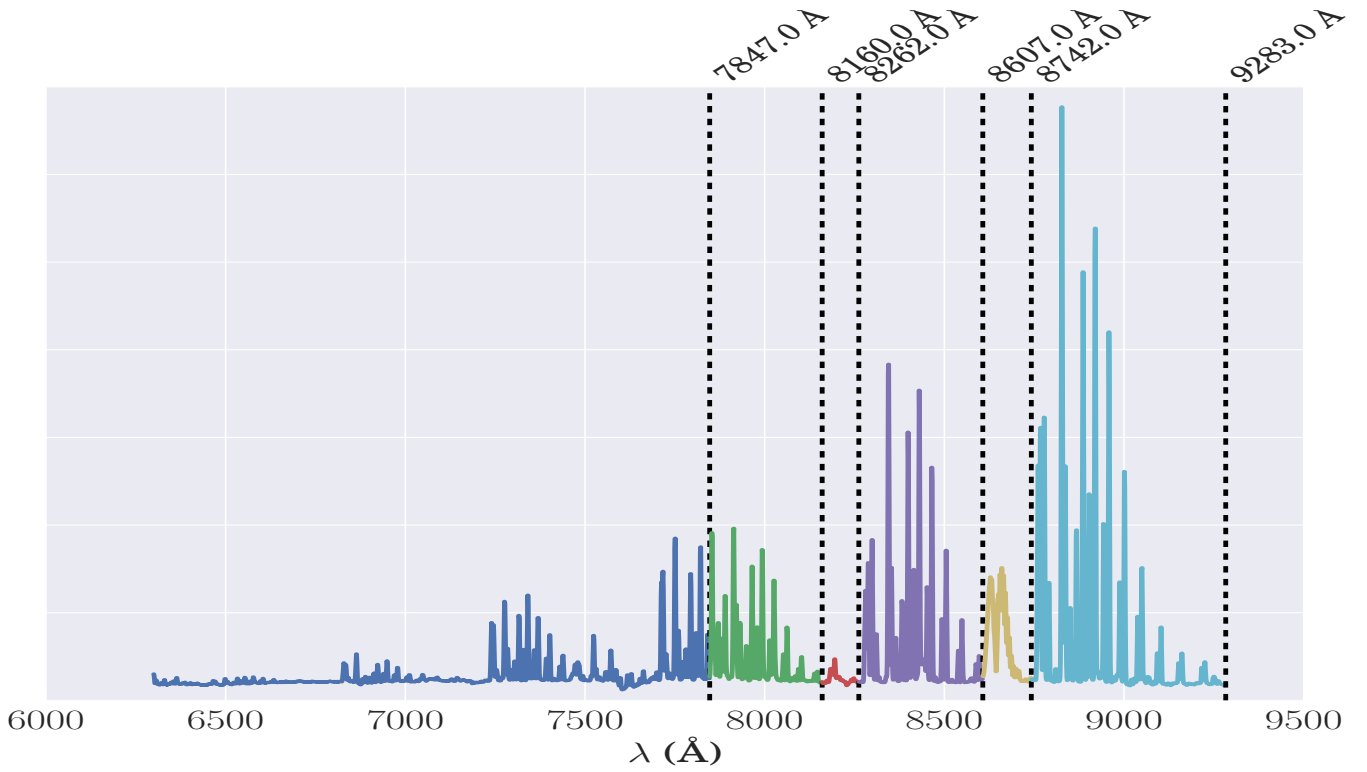


**Figure A1.** A sky spectrum from 6300 Å to 9283 Å, showing locations of split locations.

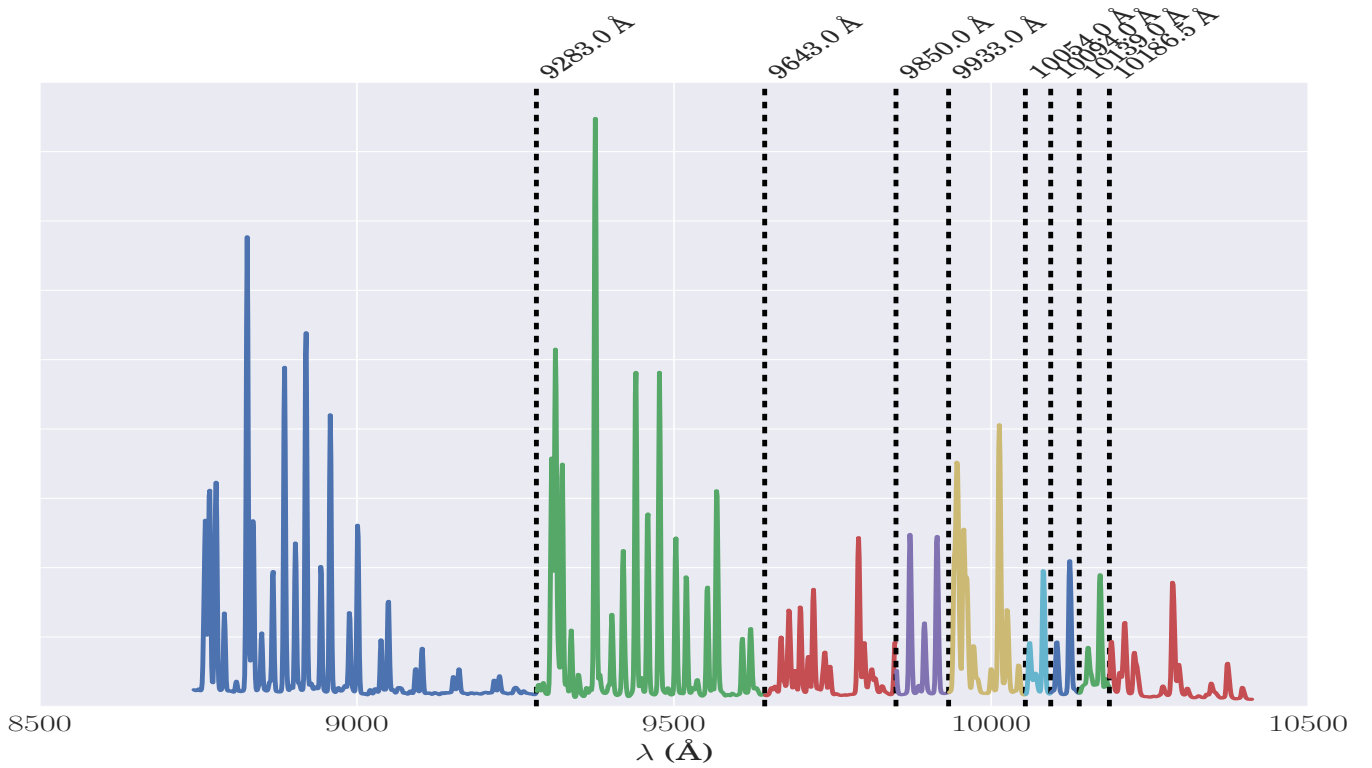


**Figure A2.** A sky spectrum centred around the Wing Ford band, showing the locations of sky splits. At the redshift of NGC 1277 and IC 843, the Wing-Ford band is observed at 10085 Å and 10160 Å respectively.

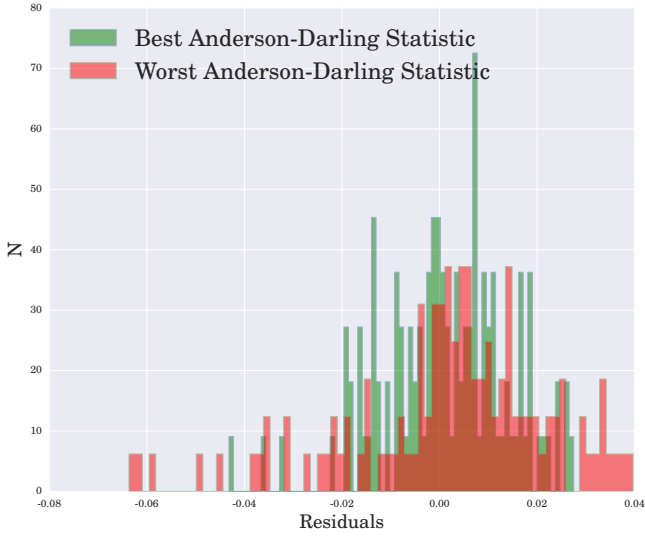


**Figure A3.** Residuals around the best fit pPXF template, for one of the NGC 1277 outer bins, after second order sky subtraction using pPXF. The two histograms correspond to two different combinations of sky line splits. The histogram in green shows the distribution with the lowest Anderson-Darling test statistic of all 32 sky split combinations, whilst the one in red shows a distribution with many outlying residuals and a large A-D statistic, corresponding to a poor second-order sky subtraction.

deviate from a normal distribution therefore imply a poor sky subtraction.

Around FeH, there are 5 wavelengths which we decided to split the sky at; 9933 Å, 10054 Å, 10094 Å, 10139 Å and 1.01865 Å. This leads to  $2^5 = 32$  possible combinations of splits. We investigated the residuals for each of these 32 combinations, both by eye and using an Anderson-Darling test (Anderson & Darling 1954, AD) with the null hypothesis that each sample was drawn from a normal distribution. The AD test is very similar to the more commonly used Kolmogorov-Smirnov test, except with a weighting function which emphasises the tails of each distribution more than a KS test does. For all analysis in this work we used the selection of sky splits with the lowest AD statistic, which corresponds to the residual distribution best described by a normal distribution with no outliers. A plot of the best (green) and worst (red) residual distribution for the NGC 1277 sky-lines is shown in Figure A3, whilst Figure A4 shows our FeH spectra for NGC 1277 and IC 843 before and after second order sky subtraction. The spectra which, by eye, have the best sky subtraction are also those with the lowest AD statistic.

## A2 A comparison of independent sky subtraction methods

Figure A5 shows equivalent width measurements of the Wing Ford band, found using spectra from the two sky subtraction processes; subtracting skylines with pPXF and median profile fitting. These methods are described in Section 3 and Appendix A.

The two methods show good agreement, implying that our FeH measurements are robust despite the challenging nature of removing residual sky emission in the far red region

of the spectrum. In particular, the global FeH measurements, on which we base our determination of the IMF in these galaxies, are entirely consistent between the two approaches.

## APPENDIX B: COMPARISON TO STELLAR POPULATION MODELS

In order to make quantitative measurements of the IMF in each galaxy, we compare our results to the CvD12 and E-MILES stellar population models. The aim is to create a spectrum with the same stellar population parameters and FeH measurement as the global spectrum for both galaxies, and then read off the IMF value of that spectrum. The two sets of models allow for changes in separate population parameters, meaning that the analysis which starts with a base template from the CvD12 models is slightly different to the case where we start with a base spectrum from the E-MILES models. Both cases are described below.

### B1 CvD12

We interpolate the base set of CvD12 models of varying IMF slope as a function of age and FeH equivalent width. These base spectra are at solar metallicity,  $[\alpha/\text{Fe}]=0$  and have solar elemental abundance ratios, whilst spanning IMF slopes from bottom-light to  $x = 3.5$ . To accurately account for the different metallicities,  $\alpha$ -abundances and  $[\text{Na}/\text{Fe}]$  ratios in each galaxy, we apply linear response functions to the CvD spectra.

The correction is defined as follows. To deal with varying continuum levels between spectra with different IMF slopes, we use multiplicative rather than additive response functions. For a spectrum with a non-solar  $\alpha$ -abundance ratio,  $S(\Delta\alpha)$ ,

$$S(\Delta\alpha) = x_\alpha S(\Delta\alpha = 0.0)$$

where  $x_\alpha$  is the linear response function. We also Taylor expand  $S(\Delta\alpha)$  to give

$$S(\Delta\alpha) \approx S(\Delta\alpha = 0.0) + \frac{dS}{d\alpha} \Delta\alpha$$

which leaves

$$x_\alpha = \left(1 + \frac{d \ln S}{d\alpha} \Delta\alpha\right)$$

We approximate the gradient term using a model spectrum from CvD12 at enhanced  $[\alpha/\text{Fe}]=+0.3$ :

$$\begin{aligned} \frac{d \ln S}{d\alpha} \Delta\alpha &\approx \frac{1}{S(\Delta\alpha = +0.0)} \frac{S(\Delta\alpha = +0.3) - S(\Delta\alpha = +0.0)}{10^{0.3} - 1} (10^{\Delta\alpha} - 1) \\ &= \left( \frac{S(\Delta\alpha = +0.3)}{S(\Delta\alpha = +0.0)} - 1 \right) \frac{10^{\Delta\alpha} - 1}{10^{0.3} - 1} \\ &= f_\alpha \end{aligned}$$

A similar correction is applied for  $[\text{Fe}/\text{H}]$  abundance variations. Because the inferred enhancements in  $[\text{Na}/\text{Fe}]$  for NGC 1277 are +0.5 dex, we use an interpolated NaMILES spectrum to approximate the gradient term, rather

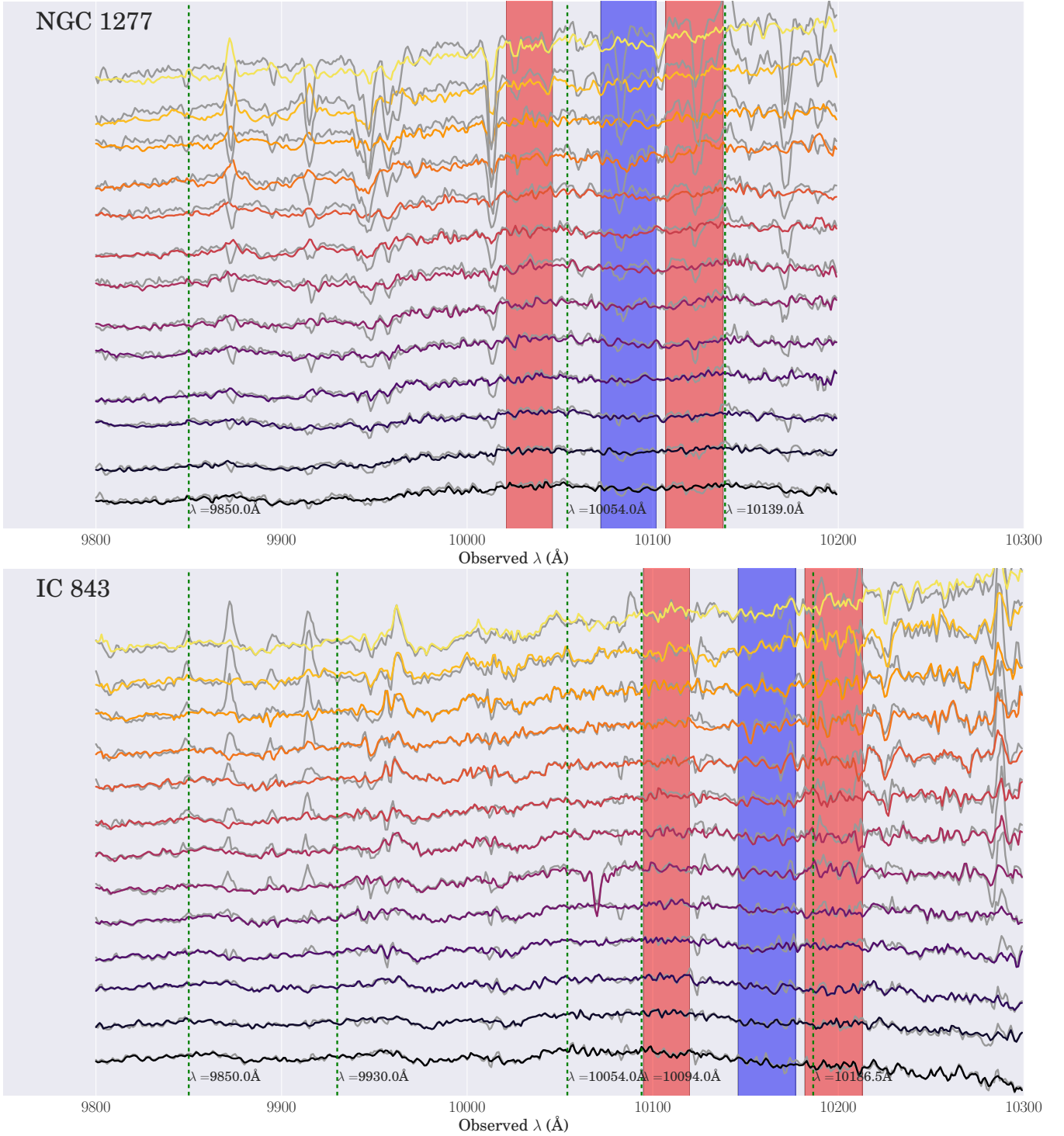


**Figure A4.** 13 spectra around the Wing-Ford band for both NGC 1277 (top) and IC 843 (bottom). These 13 spectra correspond to a central bin and 6 spectra each from the left and right sides of the galaxy. The 7 radial bins for each galaxy we use to measure index equivalent widths are formed by interpolating each of these spectra to their rest frame and adding them. The lines correspond to the spectrum in each bin before pPXF sky subtraction (but after first order sky subtraction; coloured grey) and afterwards (black through yellow). The spectra range from the central bin (bottom, dark) to the outermost (top, light). Green dashed line indicate the position of a cut to the sky spectrum. Blue shaded regions show the location of the FeH index whilst red shaded regions identify the location of the continuum regions.



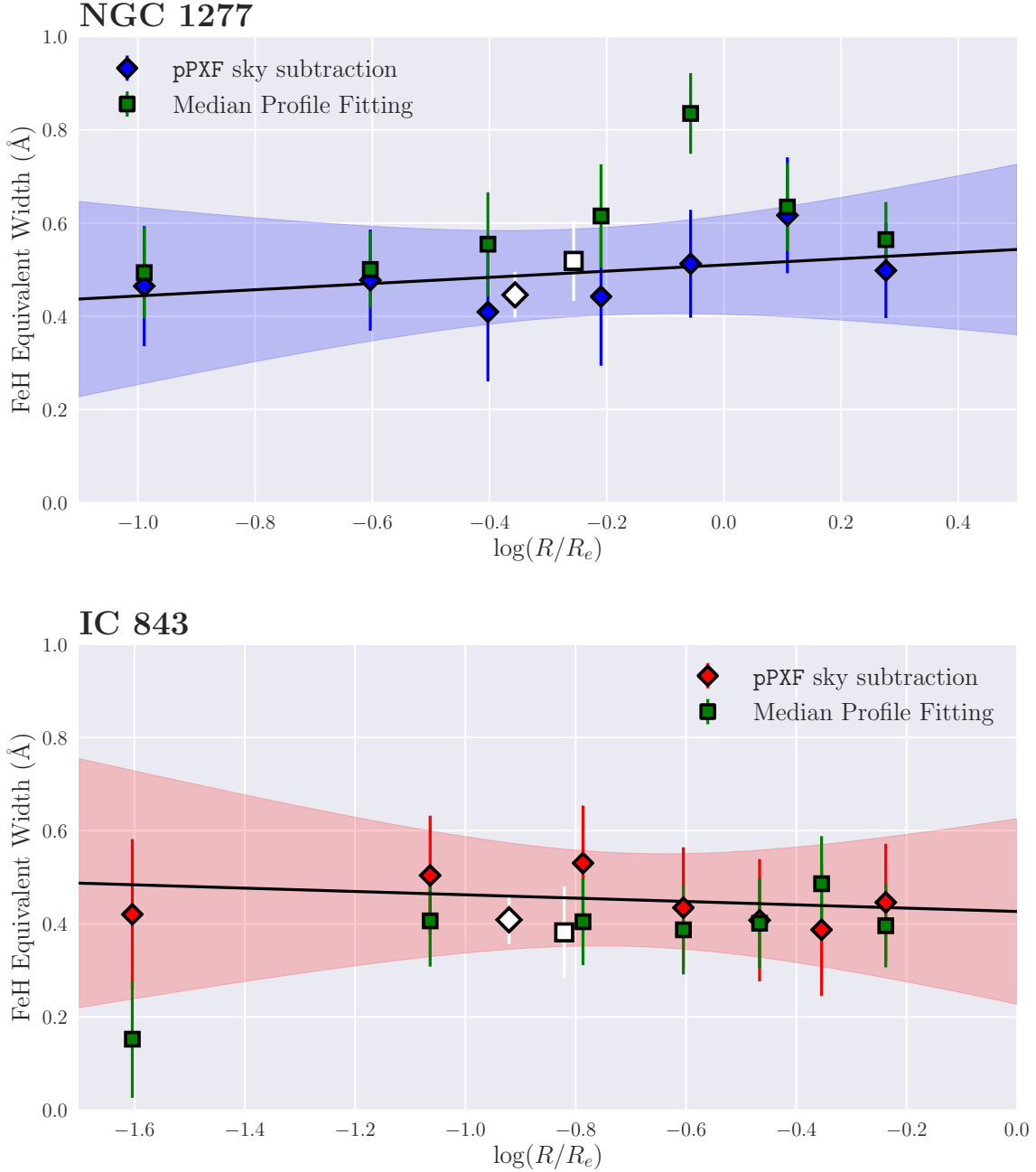


**Figure A5.** A comparison of equivalent width measurements of the Wing-Ford band, after both pPXF sky subtraction and median profile fitting, for NGC 1277 (top) and IC 843 (bottom). The best fit straight line for the pPXF sky subtraction is shown for both galaxies, as well as its one sigma uncertainty (shaded region). The two sky subtraction methods give generally good agreement, confirming the robustness of our results. In particular, the global FeH measurements on which we base our global IMF determination are entirely consistent between the two approaches.

than extrapolate from the CvD12  $[\text{Na}/\text{Fe}] = +0.3$  template. This involves converting the Na-MILES spectrum from air to vacuum wavelengths and carefully matching the spectral resolution of each set of templates before this response function is applied to the base CvD12 template.

The final set of spectra are therefore:

$$S_{\text{final}} = S_0 \cdot x_{\alpha} \cdot x_{\text{Na}} \cdot x_{\text{Fe}}$$

$$\ln S_{\text{final}} = \ln S_0 + f_{\alpha} + f_{\text{Na}} + f_{\text{Fe}}$$

It is important to note that the CvD12 spectra with non-elemental abundances (e.g those with  $[\text{Fe}/\text{H}] = +0.3$  dex) are calculated from a Chabrier IMF, whereas we find the IMFs in these galaxies from this analysis to be heavier than this. Another unavoidable source of uncertainty in the use

of these models concerns the fact that the response of the IMF sensitive indices strong in very low-mass stars (such as FeH) to quantities like  $[\alpha/\text{Fe}]$  are computed from theoretical atmospheric models which may not converge. For further discussion of this point, see CvD12 section 2.4.

## B2 E-MILES

A similar process was carried out for the E-MILES spectra. We interpolate a grid of templates of varying IMF, age, metallicity and  $[\text{Na}/\text{Fe}]$  enhancement. Since the E-MILES models are all at solar  $[\alpha/\text{Fe}]$  abundance, we use a response function from the CvD12 models to approximate an  $\alpha$ -enhanced spectrum.

A complication here is that a CvD12 model template at  $[\alpha/\text{Fe}] = +0.3$  is not at solar metallicity, because the CvD12 models are computed at fixed  $[\text{Fe}/\text{H}]$  and not fixed  $[\text{Z}/\text{H}]$ . Using the relation from [Trager et al. \(2000\)](#),

$$[\text{Fe}/\text{H}] = [\text{Z}/\text{H}] - 0.93 \times [\alpha/\text{Fe}]$$

and so CvD12 template with  $[\alpha/\text{Fe}] = +0.3$  also has  $[\text{Z}/\text{H}] = 0.279$ . We must therefore apply an  $[\alpha/\text{Fe}]$  response function to a base spectrum of metallicity

$$[\text{Z}/\text{H}]_{\text{spectrum}} = [\text{Z}/\text{H}]_{\text{galaxy}} - 0.93 \times [\alpha/\text{Fe}].$$

rather than simply  $[\text{Z}/\text{H}]_{\text{galaxy}}$ . This means, therefore, that the base template used for NGC 1277 has  $[\text{Z}/\text{H}] = 0.03$ , whilst the base template for IC 843 has  $[\text{Z}/\text{H}] = -0.197$ .

This paper has been typeset from a  $\text{\TeX}/\text{\LaTeX}$  file prepared by the author.